Painting-injection study using a virtual accelerator in a high-intensity proton accelerator

Hiroyuki HARADA

Department of Physical Science
Graduate School of Science, Hiroshima University
Kagamiyama 1-3-1, Higashi-Hiroshima, 739-8526, Japan

March 2009

Abstract

This thesis presents the painting-injection study for a high-intensity operation at the 3-GeV rapid-cycling synchrotron (RCS) of the Japan Proton Accelerator Research Complex (J-PARC). The purpose of the 3-GeV RCS is to provide 1-MW proton beam. As one of challenging aspects for the 1-MW RCS, incoherent betatron tune depressions of protons are large by the space charge force. Then the tunes of protons cross many betatron-oscillation resonance lines, which will cause potential losses of beam. It is known that the effect limits the beam intensity in the world. In order to mitigate the space charge effect, density distribution of protons should be lowered over a whole bunch. It is then required to develop the method to control the beam density.

In the transverse plane, the density distributions can be controlled in the H^- charge-exchange injection scheme. With the precise knowledge of the ring parameters and the injected beam, the footprint of the injected beam in the horizontal and vertical phase spaces in the ring can be controlled to form a uniform distribution of any size in a real space. The method which creates a uniform beam in the ring is called "painting injection". This method in a transverse plane was originally developed and established during this thesis work.

The painting injection fills the elliptical phase-space at the injection point with the injection beam by changing the injection and ring orbits during multi-turn beam injection. It is then essential to control the ring ellipse and the painting trajectories as accurately as possible. The beam commissioning system has been developed for this purpose including a virtual accelerator for efficient beam commissioning. The injection trajectories in the phase space have been confirmed by the newly developed beam -diagnostic system. The design and the measured ones agreed very well.

The painting-injection scheme established in this thesis is highly expected to provide the basic method for the study of the space-charge effect in the world because the beam emittance and distribution can be manipulated efficiently by this scheme.

Contents

List of Tables

List of Figures

1 Introduction

The science and engineering fields by making use of the secondary beams, such as neutrons, muons, kaons, neutrinos, and so on, were brought to international attention. High-intensity secondary beams can efficiently be produced by high-power proton beams. Such high intensity proton facilities have been planed and built in several places in the world. The Japan Proton Accelerator Research Complex (J-PARC)[1] is a major facility, which comprises a 400-MeV linac, a 3-GeV rapid-cycling synchrotron (RCS), and a 50-GeV synchrotron (MR). The 400-MeV H^- beam is injected into the RCS through a charge stripping foil, and the proton beam is accelerated up to 3 GeV during 20 msec. The purpose of the 3-GeV RCS is to provide 1-MW proton beam to the spallation neutron target, as well as several tens of kW proton beam to the MR.

In order to realize such a high-intensity machine, it is essential to establish a method for stable operations while keeping the beam loss as low as possible. The challenging aspects of the 1-MW RCS are as follows.

1. Due to low energy injection, incoherent betatron tune depressions of protons are large by the space charge force[2]. Then the tunes of protons cross many betatron-oscillation resonance lines, which will cause potential losses of the beam. In order to mitigate the space charge effect, density distribution of protons should be low over the whole bunch. It is then required to develop the method to control the beam density.

2. Maximum RF voltage of 450 kV per turn is necessary. Conventional ferrite loaded cavity can not produce such a high voltage under given circumstances. New type of cavity should be investigated.

3. Large aperture magnets are required so as to accommodate a large volume of proton bunch. Magnetic field interferences between adjacent magnets are then liable to occur and non-linear magnetic fields are then increased. Their effects will induce betatron-oscillation resonance lines. Optics calculations should take into account field interferences along the beam orbit.

4. Carbon stripper foil is required to be long-lived at a temperature higher than 1600 K caused by the proton of circulating beam hitting the foil. In order to achieve accelerator operations with high availability and to reduce the radiation hazard to the foil maintenance workers, lifetime of the stripper foil should be longer than 200 hours.

Amongst the above subjects, the density control method in item 1 is principally focused in this doctoral research. The method to reduce the beam density in 3-dimensional space is to utilize the painting injection in the longitudinal and transverse planes. In the longitudinal plane, the injection energy of beam is slightly modulated by the RF cavity located upstream of the injection point, and the beam is injected into the RF bucket to fill the whole bucket area. Along with this method, a higher harmonic RF cavity is used to lengthen and flatten the bunch in the beam direction. In the transverse plane, the density distributions can be controlled using the injection paint bump magnets. With the precise knowledge of the ring parameters and the injected beam, the footprint of the injected beam in the horizontal and vertical phase spaces in the ring can be controlled to form a uniform distribution of any size in the real space. This method in the transverse plane has been originally developed and established during the course of this doctoral research, and is summarized in this thesis.

The method which creates a uniform beam in the ring is called "painting injection". The painting injection fills the elliptical phase-space of the ring at the injection point by the H^- beam, whose emittance is small compared to the ring ellipse. The footprint of the H^- beam is controlled by a time-varying field so as to sweep the ellipse from center to edge or in the opposite direction. The relationship between the ring ellipse and injection beam in shown in Fig. 1. For example, when the footprints in the horizontal and vertical phase-spaces follow the functions of $\sqrt{t/T}$ and $\sqrt{1-t/T}$, respectively, the beam forms a uniform distribution in the 2-demension real space. Here, T is the total injection time. In the painting injection process, the carbon stripping foil for the charge exchange is installed at the edge of the ring ellipse in order to minimize the scattering of the circulating beam. The beam track control of horizontal phase-space coordinate is performed by eight bump magnets installed in the injection section of the ring and that of vertical phase-space coordinate is performed by two bump magnets installed in the beam injection transport line. As seen in Fig. 1, it is essential to accurately identify the ring parameters and control the beam trajectories in the injection line and the ring. An efficient beam control system is then indispensable.

Large-scale and high-intensity accelerators such as J-PARC typically comprise more than hundreds of devices, and the control system is required to manage all the devices in a unified manner. Also in order to efficiently perform the beam commissioning and the parameter measurements on beam and accelerators, the control system should be provided with functions that facilitate the development of beam commissioning tools. Such a control sys-

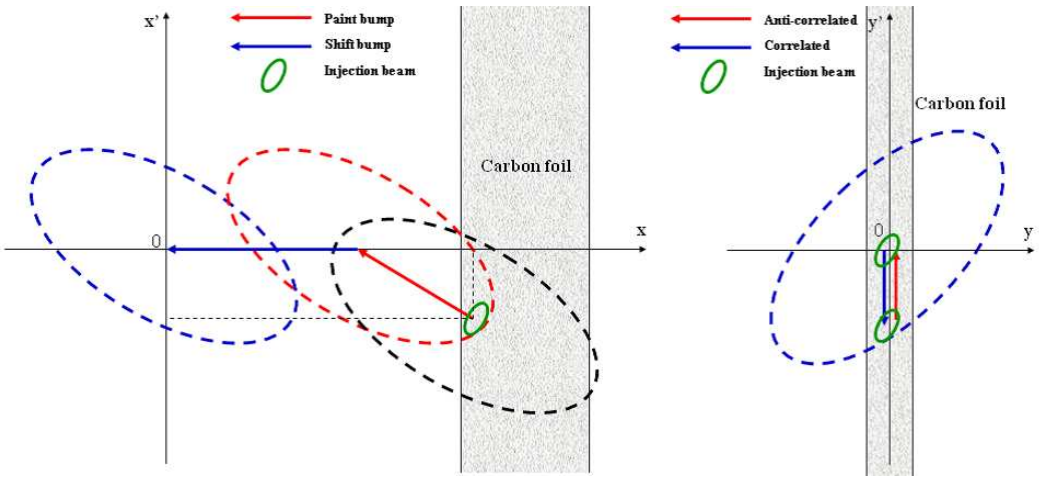

Figure 1: Horizontal(left) and vertical(right) painting-injection

tem has been constructed by software toolkits and applications based on the Experimental Physics and Industrial Control System (EPICS)[3] and it has given operators easier construction of commissioning tools because operators can identify and control all devices by the record name in the input/output controller (IOC) regardless of the device types. The beam-commissioning tools are constructed for each commissioning stage such as injection- and extraction-line tuning, a closed-orbit distortion correction, optics corrections, and so on. Those tools utilize the functions of the virtual accelerator (VA), where the VA is defined as an on-line accelerator model with beam diagnostic devices. The VA is configured under the EPICS IOC for the VA in parallel with the real accelerator (RA). The control system including the VA is shown in Fig. 2. The VA calculates the beam characteristic using the RA parameters received from the EPICS IOC as well as any machine parameter set the operator wants to investigate. Parameter sets that the model used also are available for a RA operation through the EPICS IOC. Each commissioning tool is responsible for the specified VA parameters, such as optics correction tools for dipole and quadrupole magnet fields with higher-order components, injection-line tuning tool for injection bump magnet fields, and so on. The VA parameters thus obtained are commonly used by all the commissioning tools. This control scheme with VA enables very efficient beam-commissioning activities. First of all, it greatly facilitates the development of beam-commissioning tools. They can always be debugged and/or tested by running the VA for a virtual commissioning. And, once completed, they are easily converted to those for the RA by changing the suffix of each record

name from VA to RA, and consequently the VA greatly decreases the debugging time. Another aspect of this system is, for example, that new magnet parameters for the RA operation can be checked by the VA whether they are acceptable from the view point of aperture clearance. Only acceptable, the parameters are transferred quickly to the actual RA operation through the IOC. In the beam physics study with the RA, the experimental conditions can clearly be identified beforehand, and the results can then be examined by using the RA. We have developed this VA and beam-commissioning tools for the beam physics study of the RCS. The VA and the tools are used for control of ring parameters and painting study.

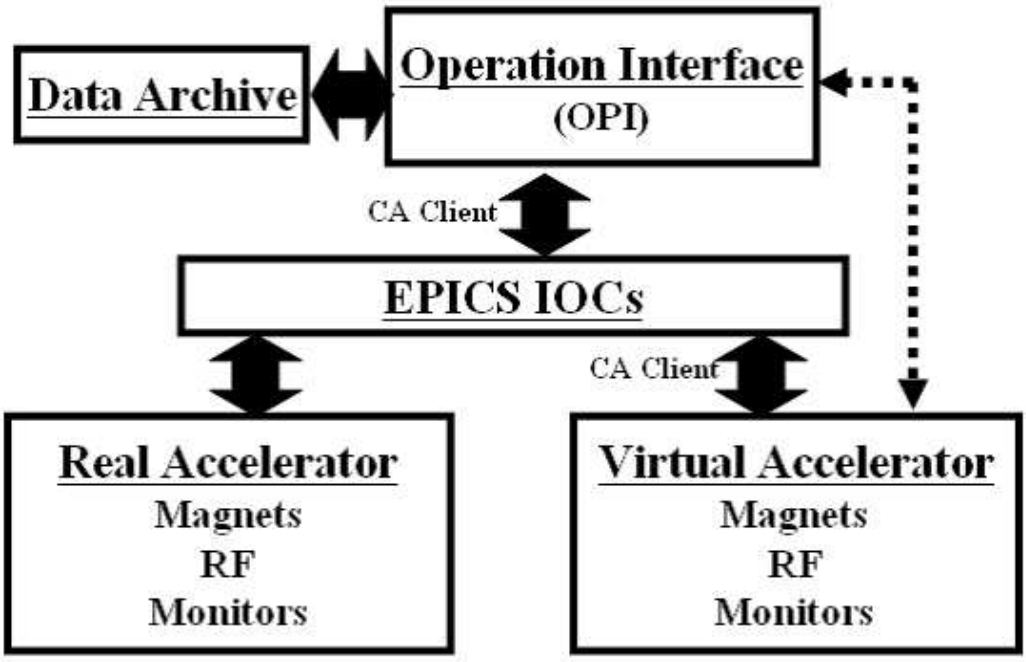

Figure 2: Control system including virtual accelerator

In the following sections, the outline of J-PARC facility and the VA is provided in Section 2, beam commissioning using the VA is discussed in Section 3, painting-injection study is discussed in Section 4, and summary and conclusion is provided in Section 5.

2 Construction of Virtual accelerator

Efficient control systems are essential for the operations of the large-scale and high-intensity accelerators. Such accelerators typically comprise more than hundreds of devices, and the beam-commissioning systems are required to manage all the devices in a unified manner. For low-loss operations, all the magnet parameters should be occasionally examined during the accelerator operation, whether they are acceptable. In addition, the experimental conditions under which the accelerator measurements should be performed must be clearly specified in order to obtain accurate data in the most efficient manner. Such a control system has been realized by implementing the virtual accelerator (VA) under the Experimental Physics and Industrial Control System (EPICS) input/output controller (IOC)[3] in parallel with the real accelerator (RA).

The J-PARC 3-GeV RCS introduced at Section 2.1 is controlled using the above-mentioned VA control system. Since the VA is provided with virtual beam diagnostic devices, it can simulate beam reactions for various kinds of measurements and it helps to construct the commissioning tools for the RA without using a real beam.

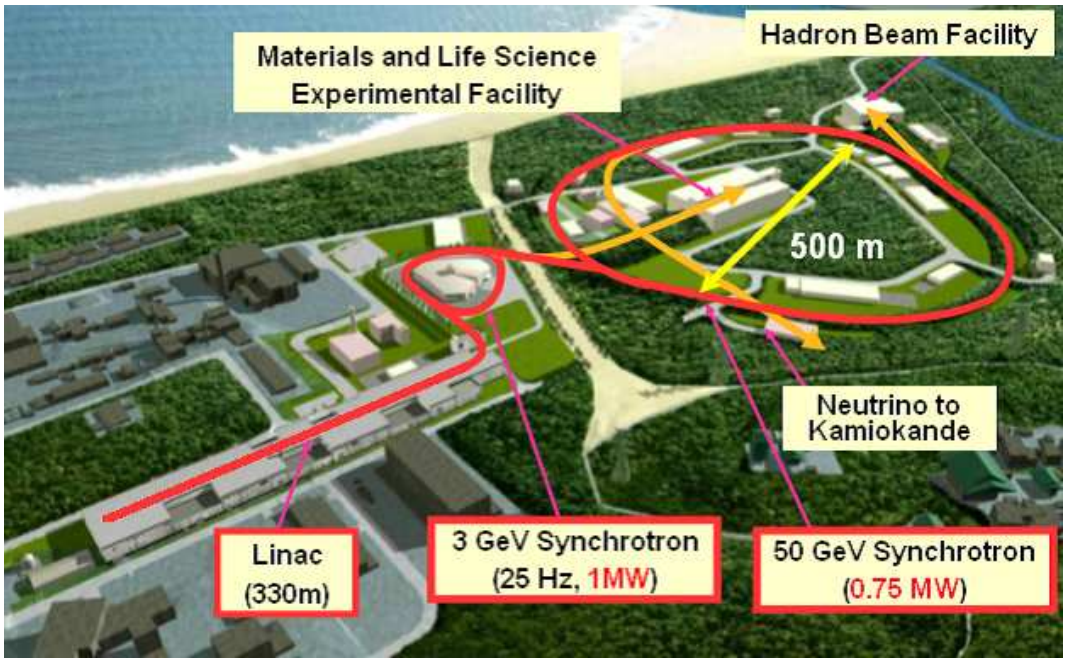

Figure 3: J-PARC Facility

2.1 Japan Proton Accelerator Research Complex (J-PARC)

This section describes the high-intensity proton accelerator facility in Japan, which is now referred to as J-PARC project (Japan Proton Accelerator Research Complex)[1] jointly operated by the JAEA (Japan Atomic Energy Agency) and the KEK (High Energy Accelerator Research Organization). The facility comprises a 400-MeV linac[4], a 3-GeV rapid-cycling synchrotron (RCS), and a 50-GeV synchrotron (MR)[5] as shown in Fig. 3. The 400-MeV beams from the linac are injected to the RCS. The RCS accelerates the beam up to 3 GeV with a period of 20 msec and provides to the Material and Life science Facility (MLF) or the MR with a repetition rate of 25 Hz, which a beam power is 1 MW. The MR provides a beam power of 0.75 MW with a period of 3.64 s to either the fundamental and nuclear physics experimental area or the neutrino production target. The beams are slowly extracted to the former, while they are fast extracted to the latter. At the first stage, the energy of the linac and MR is 181 MeV and 30 GeV, respectively. More specifically, main beam parameters are summarized in Table 1.

The purpose of the project is to promote all the related scientific and engineering fields, by making the full use of the secondary beams, including neutrons, muons, kaons, neutrinos, and so forth, which can be efficiently produced by the proton beams. In order to produce the intense secondary beams, the beam power should be as high as possible, while the beam energy should sufficiently exceed the thresholds for the efficient production of the secondary beams.

Table 1: Main Beam Parameters. *:Parameters at the first stage

Linac	
Ions	Negative Hydrogen(H^-)
Energy for RCS injection	400(181*) MeV
Peak Current	50 mA
Beam Pulse Length	500 μsec
Repetition Rate	50 Hz
RCS	
Injection Beam Energy	400(181*) MeV
Extraction Beam Energy	3 GeV
Injection Time	500 μsec
Repetition	25 Hz
Average Beam Current	333 μA
Extraction Scheme	Fast
MR	
Injection Beam Energy	3 GeV
Extraction Beam Energy	50(30*) GeV
Repetition	0.3 Hz
Average Beam Current	15 μA
Extraction Scheme	Fast, and Slow

2.1.1 3-GeV Rapid-Cycling Synchrotron (RCS)

The 3-GeV Rapid-Cycling Synchrotron (RCS) has a threefold- and mirror-symmetric lattice over its circumference of 348.333 m. The global layout of the RCS is shown in Fig. 4. Main design parameters of the RCS are summarized in Table 2. The injection and extraction beam energy is 400 MeV and 3 GeV, respectively. The target of the RCS is to provide the beam power of 1 MW with a repetition rate of 25 Hz. This section describes the design of the beam optics and the injection scheme at the RCS.

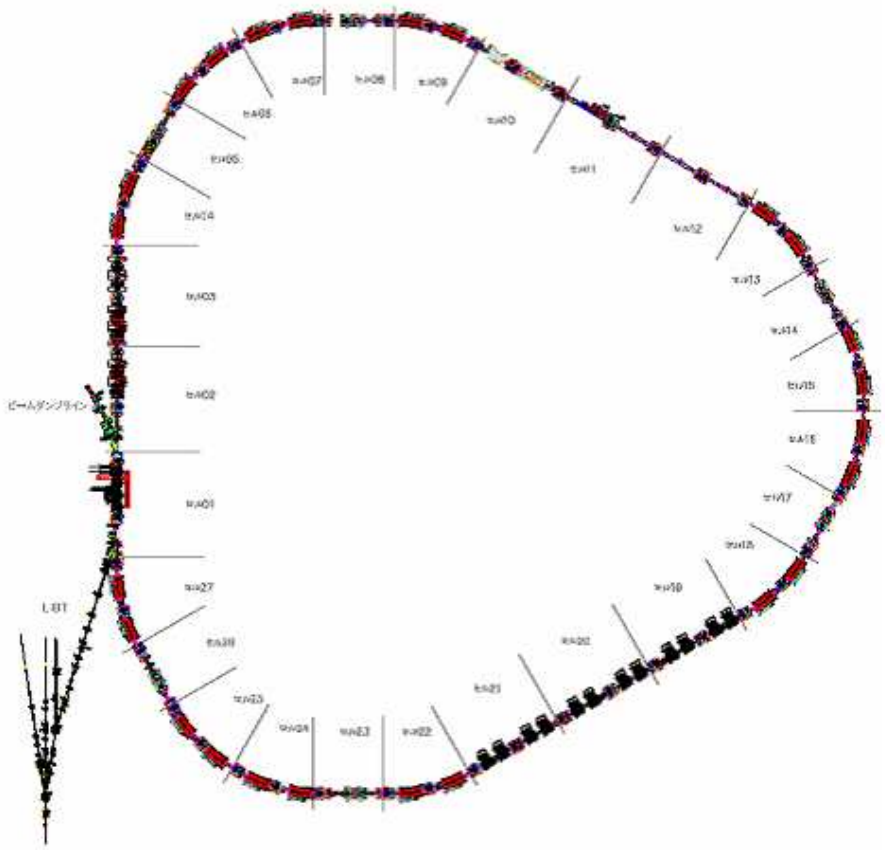

Figure 4: Layout of 3-GeV RCS

Table 2: Main parameters of 3-GeV RCS

Parameter	Value
Circumference	348.333 m
Average Radius	55.44 m
Injection Beam Energy	400(181) MeV
Extraction Beam Energy	3 GeV
Output Beam Power	1 MW
Particles Per Pulse	$8.3 \times 10^{1}3$ ppp
Revolution Period at Injection/Extraction	1.629(2.129)/1.196 μsec
Repetition	25 Hz
Injection Time	500 μsec
Average Current	333 μA

2.1.2 Beam Optics at RCS

The RCS has a threefold-symmetric lattice and is composed of 24 bending magnets and 7 families 60 quadrupole magnets[6]. Each super-period consists of two 3-DOFO modules with missing bends and a 3-DOFO insertion. Fig. 5 and 6 show the magnet arrangement and main optics parameters in a super period. Each arc module has a missing-bend cell, where the horizontal dispersion function has the maximum value, raising the transition gamma to 9.14 compared to normal FODO lattices for an easier RF[7] operation. The missing-bend cells are suitably utilized for chromaticity correction with sextupole magnets. The three insertions have no dispersion as the straight section for beam injection[8], extraction[8] and RF acceleration, respectively. Main lattice parameters are summarized in Table 3. The nominal operating point for betatron tunes is (6.68, 6.27).

The beam emittance, collimator aperture and the ring aperture are summarized in Table 2.1.2. The collimator system[9] at the RCS is installed at the downstream of the injection section in order to localize the beam loss in the ring. While the painting beam emittance and the collimator acceptance are controlled to 216 π and 324 π mm mrad, respectively, the physical aperture is at least 486 π mm mrad for the entire ring. The ring also accepts the beam momentum spread up to $\pm$ 1%.

Table 3: Main lattice parameters of 3-GeV RCS

Parameter	Value
Super Periodicity	3
Unit Period	Insertion + Arc
Operating Point(ν_x, ν_y)	(6.68, 6.27)
Maximum β Function (X/Y) in Arc	26.3/26.3 m
Maximum η Function in Arc	5.555 m
Maximum β Function (X/Y) in Insertion	26.3/26.3 m
Maximum η Function in Insertion	0.0 m
Chromaticity (X/Y) w/o nonlinear fields	-8.5/-8.8
Transition gamma	9.14
Momentum Compaction	0.012

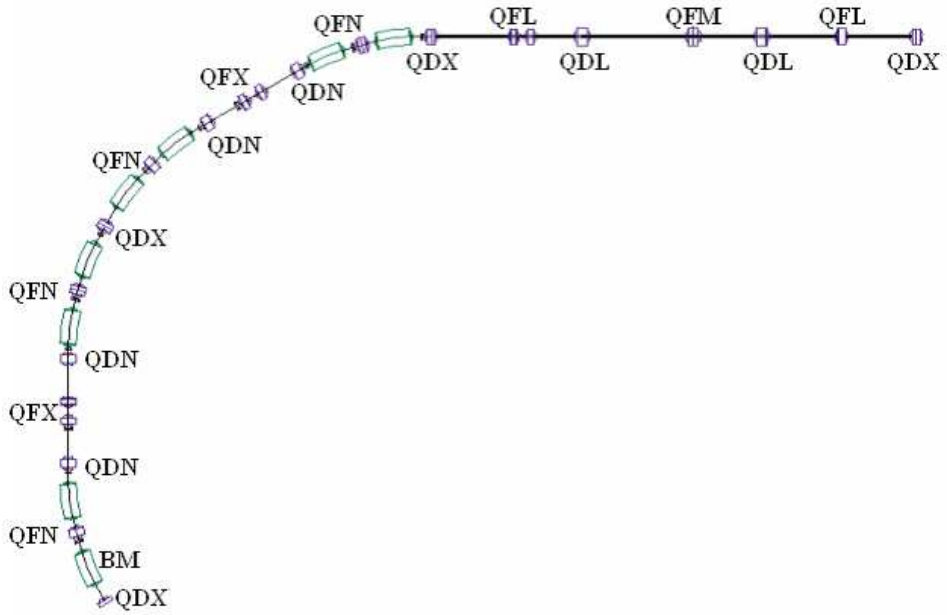

Figure 5: Arrangement of main magnets for a super period

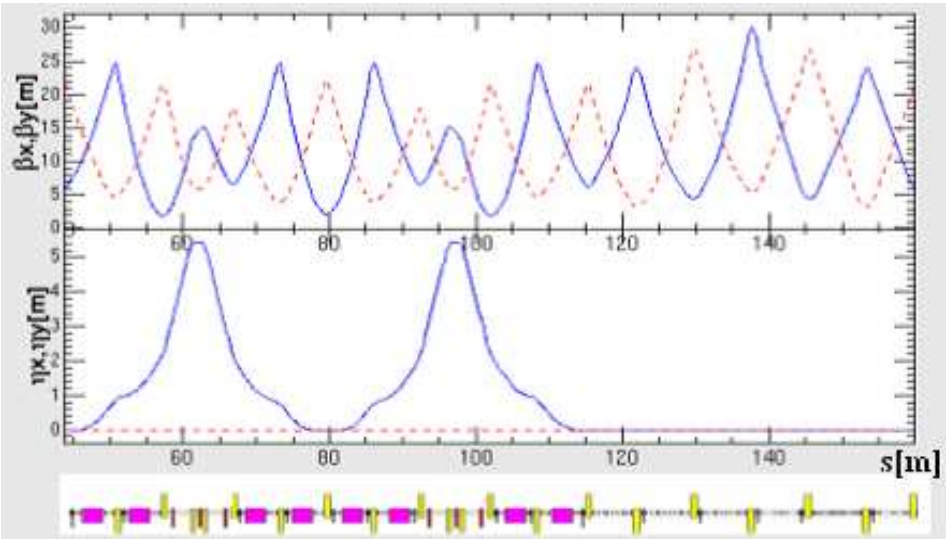

Figure 6: Main optics parameters for a super period. Beta functions β are plotted at the first trace; dispersion functions η, at the second trace. Solid lines are for horizontal direction; and dashed line, for vertical direction.

Table 4: Main beam emittance and aperture of 3-GeV RCS

Parameter	Value
Transverse Emittance of Injection Beam	4 π mm mrad
Painting Emittance	216 π mm mrad
Collimation Aperture	324 π mm mrad
Physical Aperture	$\geq$ 486 π mm mrad
Dynamic Aperture	$\geq$ 486 π mm mrad
Longitudinal Emittance	3.5 eVs

2.1.3 Injection scheme at RCS

The H^- beams produced in the negative ion source are accelerated in the Linac and the beams are chopped with a normal chopping rate of 54 %. The RCS injection adopts the H^- foil-stripping charge-exchange injection. The H^- beams from the Linac are injected to the RCS during the injection time of 500 μsec, corresponding to the multi-turn injection of 308 or 235 turns for injection energy of 400 or 181 MeV.

In the horizontal plane, the scheme consists of two septum magnets (ISEP1,

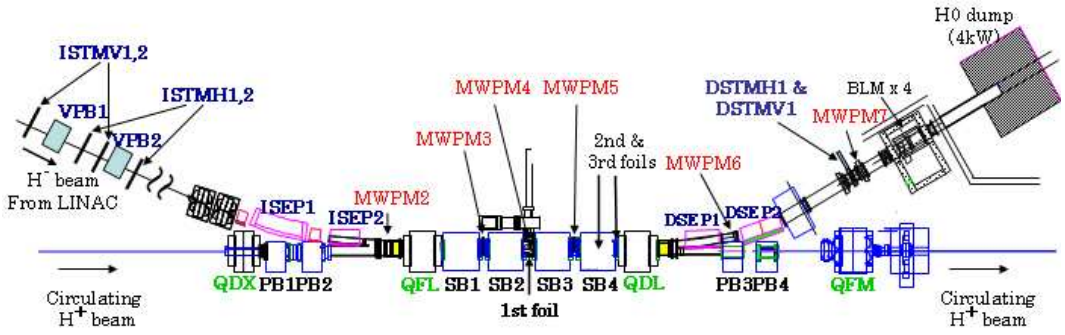

Figure 7: Layout of the RCS injection to dump line

2) in the beam-transport line, two septum magnets (DSEP1, 2) in the beam-dump line, two steering magnets (ISTMH1, 2) in the beam-transport line, one steering magnet (DSTMH1) in the beam-dump line, four main orbit bump magnets (SB1$\sim$4), and four other orbit bump magnets (PB1$\sim$4). The SBs are installed with a shift of 95 mm for the reference orbit in a drift space between the focusing magnet(QFL) and defocusing one(QDL), and each SB has a split-type structure for install of foil system and are excited by a single power supply. Other magnets are excited by their own power supplies. First

two of PBs are installed at the upstream QFL and the other two are at the downstream of the QDL. In the vertical plane, two orbit bump magnets (VPB1, 2) for painting injection and two steering magnets (ISTMV1, 2) are installed in the injection line and one steering magnet (DSTMV1) is installed in the dump line[8][10][11]. The system is shown in Fig. 7. The 99.9 % of incoming H^- beam is stripped to H^+, and is injected into the ring. The unstripped beams (H^0 and H^-) are finally stripped to H^- at the downstream second and third foils. In Fig. 7, MWPM stands for multi-wire profile monitor[12], which detects the injected-beam shapes and positions for horizontal and vertical directions.

The painting injection fills the elliptical phase-space at the injection point with the injection beam by changing the injection and ring orbits during multi-turn beam injection. The normal beam orbits at injection section for painting and center injection in horizontal direction are shown in Fig. 8 and 9, respectively. The center injection is also needed for the beam study using the small beam size in an operation of the low-current beam. As the painting-injection scheme for horizontal direction, the closed orbit of the ring is swept from the center to the edge for long-axis direction of a beam ellipse in the phase space at injection point by using the decay pattern of the magnetic field of these PBs. The injection of vertical direction has the scheme of painting and center injection, too. For the painting injection, the injection angle of vertical direction at injection point is directly swept so as to paint the beam from center to edge or edge to center by the two VPBs installed at a beam-transport line.

The Linac provides a pulsed beam (called macro pulse) with 500 μsec. The chopped beam (called intermediate pulse) with a chopping factor of 54 % within the macro pulse are injected into two RF buckets in the RCS. The schematic image is shown in Fig. 10. The current or particles per pulse in the RCS is variable by the peak current, macro-pulse length and the chopping factor. In the stage of beam commissioning, the particles per pulse is reduced to the 1 % of the design intensity in order to avoid the beam loss corresponding to the residual radioactivities. As the nominal parameters of Linac in the first beam commissioning, the peak current, macro-pulse length, chopping factor and number of beam bunches is 5 mA, 50 μsec, 54 % and 1 bunch, respectively. The chopping factor corresponds to the momentum spread of the captured beam from the synchrotron oscillation in the ring. The momentum spread is variable by the chopping factor and RF voltage.

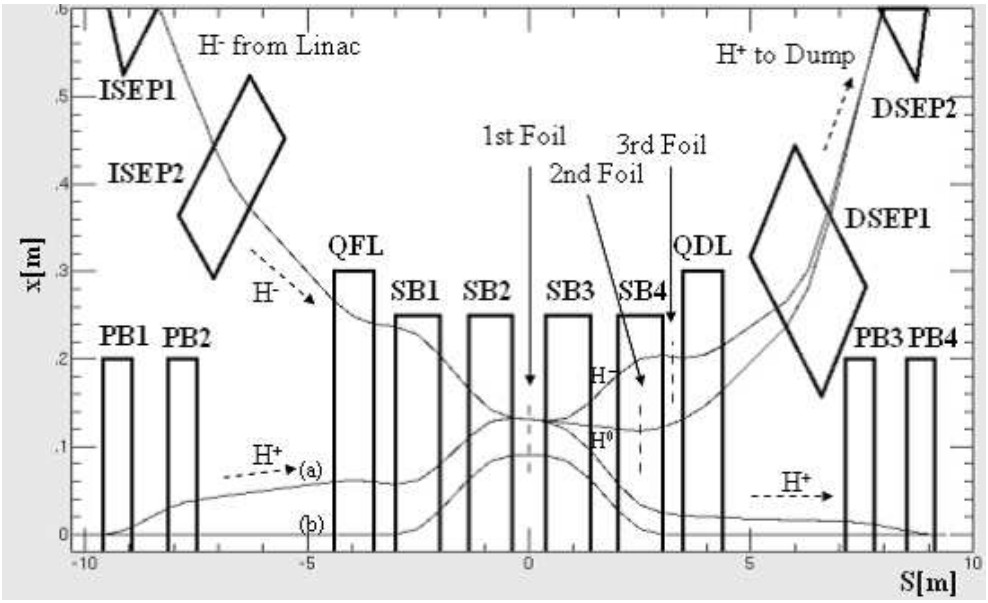

Figure 8: Beam orbits of painting injection at injection section. (a):Painting start, (b):Painting end.

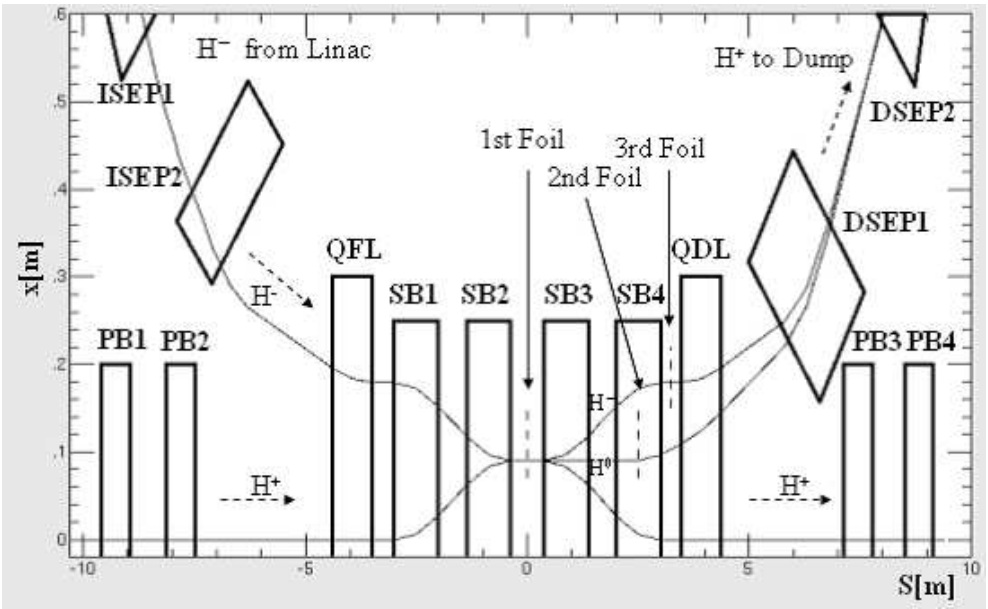

Figure 9: Beam orbits of center injection at injection section

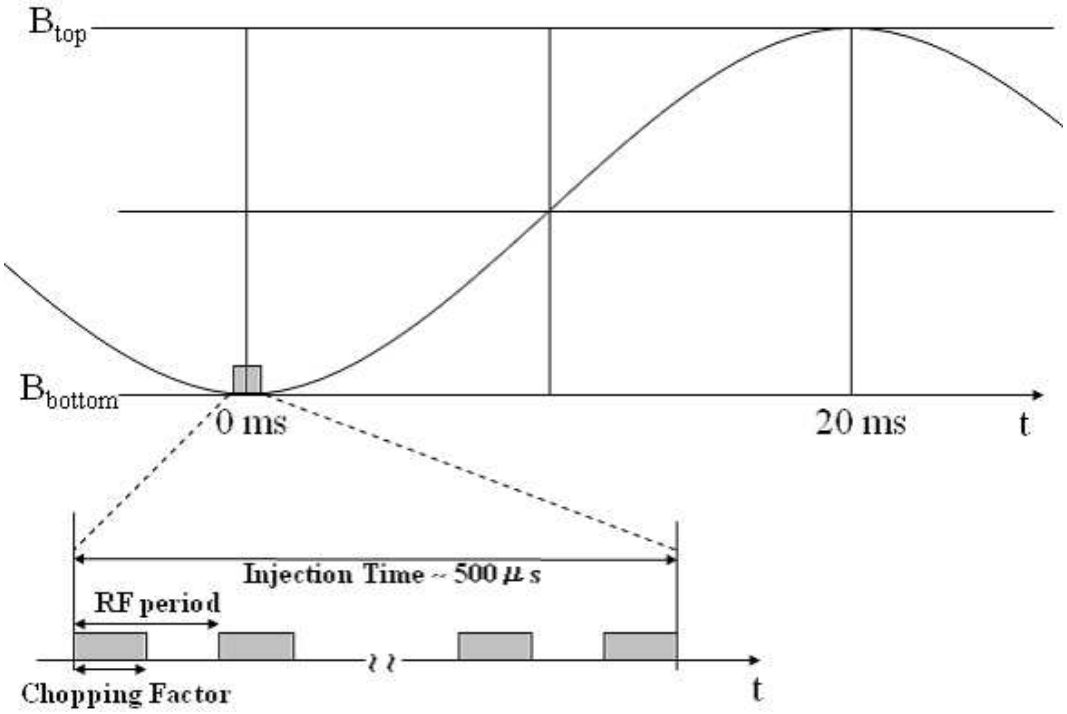

Figure 10: Schematic view of multi-turn injection

2.2 Beam commissioning system based on virtual accelerator

A logical accelerator called the virtual accelerator (VA) enables very efficient commissioning and operation of an accelerator. The VA presented here is a beam simulator where a beam monitor scheme is added to the online model and is configured in the EPICS IOC in parallel with a RA. We have constructed a beam commissioning system based on EPICS IOC including a VA at the 3-GeV RCS in J-PARC.

The EPICS[3] is a set of open-source software tools, libraries, and applications and has been developed collaboratively and used worldwide to create control systems for scientific instruments such as particle accelerators and telescopes and large scientific experiments. Such distributed control systems typically comprise tens or even hundreds of computers. The EPICS uses client/server and publish/subscribe architectures to communicate with various computers. The IOC performs real-world I/O and local control tasks and publishes this information to clients using the channel access (CA) network protocol. An advantage of the EPICS is that the development of applications

by physicists is easy because they can only see the record in IOCs for the accelerator hardware. By using the channel access client (CA Client), it is possible to read/write (I/O) the set values of the current operation from/to the records in IOCs via a network without depending on the type of hardware.

The beam commissioning system including the VA is shown in Fig. 11. The operation interface (OPI) with a graphical user interface (GUI) and the CA client is an application to plot various types of data and to control devices through the IOC. The set value of magnets and the measured beam data in the OPI are stored in the data archive and the data are recalled with the time stamp.

The VA is provided with beam diagnostic devices such as a beam position monitor (BPM) to detect the transverse beam position at every turn or the averaged closed orbit, a beam profile monitor to measure the transverse profile in the ring, a beam current monitor to detect the bunch shape, and the beam loss monitor to identify the loss points in the ring. As for a precise description of magnets, the measured nonlinear components and interference fields are included in the VA.

The OPI and VA have been created using SAD[13]. SAD is a computing

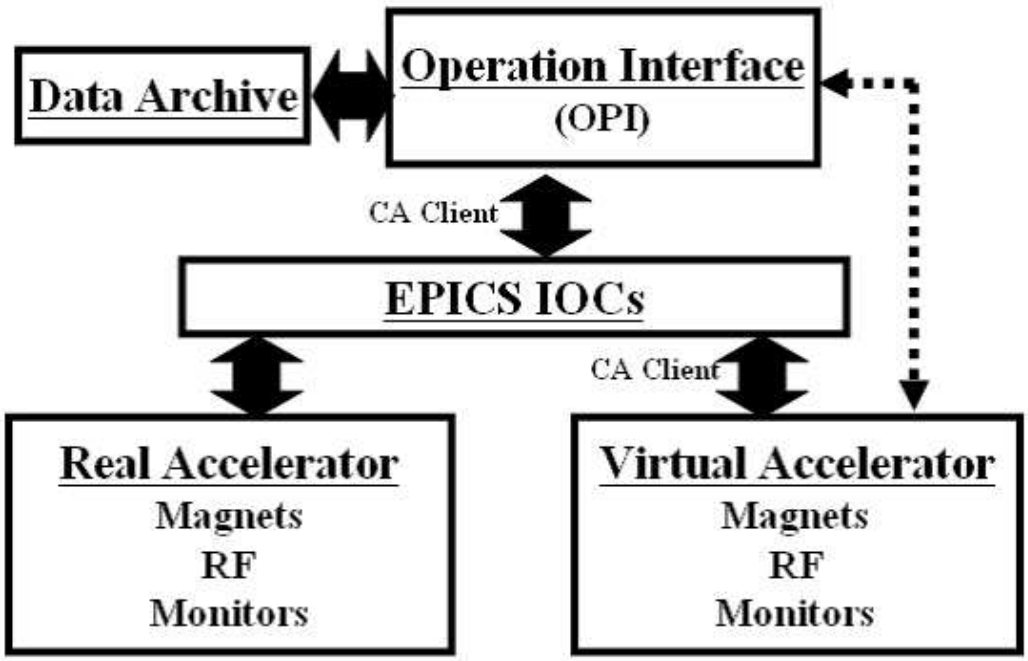

Figure 11: Control system including virtual accelerator

program that has been developed at KEK since 1986 for designing, simulating, commissioning, and improving accelerators. Major functions of SAD include structural definitions of beam-lines and components[14], rich matching functions (optics, optical/geometrical, off-momentum, finite-amplitude and spin matching), SAD script programming interface like Mathematica[15] style, 6D full-symplectic particle tracking, Taylor map by automatic differentiation and lie algebraic map for nonlinear analysis with the higher-order nonlinear components up to the normal and skew 42-pole magnetic field component, emittance calculation using 6D beam-matrix method and anomalous emittance calculation[16], a GUI application based on Tkinter (Tcl/Tk)[17] and EPICS CA client capability such as CaWrite, CaRead, and CaMonitor that imply write, read, and subscribe to a record in an IOC, respectively. Additional packages SAD includes are an envelope model calculation and a multi-particle tracking with space charge force.

The OPI and VA exchange the information via the IOC. The records with memory space are defined in the IOC and are identified by the record names. For example, the steering magnets are controlled in the following. The records for the kick angles of the steering magnets in the RA and VA are defined as "RA:STM01:ANGLE" and "VA:STM01:ANGLE," respectively. The kick angle of a steering magnet is transferred from the OPI to the IOC. In the RA, the angle is converted into a current by the measured magnetic field and the current is set into the power supply of the steering magnet. In the VA, the angle is set into the magnet without conversion.

As another usage of the VA, the OPI can directly call the VA as the online model. For example, the initial parameters of the quadrupole magnets for the given betatron tune are calculated by the online model and the OPI plots the beta and dispersion functions for the quadrupole strengths.

Most of the components in the RA and VA can have communication based on EPICS. However, some of components in the RA are still communicating by the file transfer. These communication paths should be revised in the near future to use the EPICS.

2.3 Construction of accelerator model

The accelerator components are the bending and quadrupole magnets as the main component, sextupole magnets, drift spaces, beam monitors, RF cavities, and so on. The magnetic-field strength and length for all components around the RCS ring are defined in the accelerator model. It is important to construct the accelerator model to be calculable online and reflect the RA for the VA. The magnetic field of the magnets has been measured before they are installed in the RCS tunnel and these magnets are modeled based on the measured magnetic field. It is important to estimate the higher-order components for the main magnetic component in this modeling of magnets because the main component can be controlled by the input current value from the power supply but the higher-order components that may give the dynamic aperture the effect cannot be directly controlled. This section describes the construction of accelerator model for the bending magnet[18], quadrupole magnet[18] and shift-bump magnet.

2.3.1 Bending magnet as deflecting magnet

For the bending magnets, the magnetic fields B_y for vertical direction are measured by the short coil with mapping in three dimension (x, y, s). The effective length L_{BM} is derived from

$$L_{BM} = \frac{\int_{-\infty}^{\infty} B_y(s)_{(x,y=0)} ds}{B_y(c)_{(x,y=0)}}, \tag{2.1}$$

where $B_y(c)_{(x,y=0)}$ is the magnetic field at the center of bending magnet. The total magnetic field $B_y L_{BM}$ is performed the multi-pole expansion for horizontal plane (y=0) by the Polynomial fitting and the magnetic-field expansion for three dimensions is described at Appendix A. The Polynomial fitting is

$$B_y L_{BM(y=0)} = bl_0 + bl_1 x + bl_2 x^2 + bl_3 x^3 + \cdots + bl_n x^n, \tag{2.2}$$

and consequently the main and higher-order components of the bending magnet are derived from bl_n and

$$K_n = \frac{1}{(B\rho)} \int (\frac{\partial^n B_y}{\partial x^n}) ds = \frac{n!}{(B\rho)} bl_n, \tag{2.3}$$

and

$$(B\rho) = \frac{1}{0.3} p, \tag{2.4}$$

where K_n is the n-order magnetic-field component and p is the momentum. The derived main component K_0 of the bending magnet is defined as the element of effective length L_{BM} into the accelerator model. The higher-order components of the bending magnet are derived up to 12-pole components and they are defined as the thin-lens element at both ends (upstream and downstream) of the bending magnet. The length of fringe field, which is described in Appendix B, is derived from the field distribution for the beam direction and is defined as $F1$ into the model. The fringe field has a defocusing and sextupole-like field component. The magnetic wedges for the reference orbit at entrance and exit edges are defined as $E1$ and $E2$ with half of bending angle, respectively. The magnetic wedge has a defocusing field component.

2.3.2 Quadrupole magnet as focusing/defocusing magnet

For the quadrupole magnets, the magnetic fields B_y for vertical direction are measured by the short coil with mapping in three dimension (x, y, s). The effective length L_{QM} is derived from

$$L_{QM} = \frac{\int_{-\infty}^{\infty} \frac{\partial B_y(s)}{\partial x}|_{(x,y=0)} ds}{\frac{\partial B_y(c)}{\partial x}|_{(x,y=0)}}, \tag{2.5}$$

where $\frac{\partial B_y(c)}{\partial x}|_{(x,y=0)}$ is the quadupole-field component at the center of quarupole magnet and is defined as b_1 in Eq.2.6. The field expansion for the focusing/defocusing magnet is given by

$$B_y + jB_x = \Sigma_{n=0}^{\infty} b_n (x+jy)^n - \frac{b_0''}{2} y^2 - \frac{b_1''}{2}(x+jy)y^2 + \cdots \tag{2.6}$$

with

$$b_n^{(m)} = \frac{\partial^m b_n}{\partial s^m} \tag{2.7}$$

where j is $\sqrt{-1}$. From Polynomial fitting of Eq.2.2, the main component b_1 and higher-order components b_n ($n \geq 2$) are derived. The derived main field strength K_1 of the quadrupole magnet is defined as the element of effective length L_{QM} into the accelerator model. The higher-order components of the quadrupole magnet are derived up to 20-pole components and they are incorporated in the model as the thin-lens element at both ends (upstream and downstream) of the magnets. The fringe field for the quadrupole magnet is denoted as the parameters of $F1$ and $F2$,

$$\begin{aligned} F1 &= \sqrt{|\ 24(I_0^2/2 - I_1)\ |} \\ F2 &= I_2 - I_0^3/3 \end{aligned} \tag{2.8}$$

where

$$I_n = \int (s - s_0)^n \frac{K1(s)}{K1(0)} ds,$$

and their parameters have a sextupole-like component $\frac{b_0''}{2} y^2$ and octupole-like component $\frac{b_1''}{2}(x+jy)y^2$, respectively. The quadruple magnets has no the magnetic wedge for the reference orbit at entrance and exit edges.

2.3.3 Shift-bump magnet for beam injection

The four shift-bump magnets are powered by single power supply during beam-injection time of 500 μsec. The shift-bump magnets with a large aperture are closely installed between quadrupole magnets (QFL and QDL). Consequently, the measured field of these magnets causes interference, as shown in Fig.12. Field measurements have been performed separately for magnet pairs such as two shift-bump magnets and a pair of shift bump and quadrupole magnet. The results were then joined together to produce the whole field from QFL to QDL in the figure. The injected beam passes through a far side of the magnet apertures, where the nonlinear fields may cause some betatron resonances for the circulating beam during the injection period. The measured magnetic-field B_y in Fig.12 is divided into 20mm segments along the beam direction. The magnetic field in each segment was expanded by a Polynomial fitting up to decapole component, and is incorporated into the accelerator model as a magnet with a 20mm effective length with a shift of 95 mm for the reference ring-orbit.

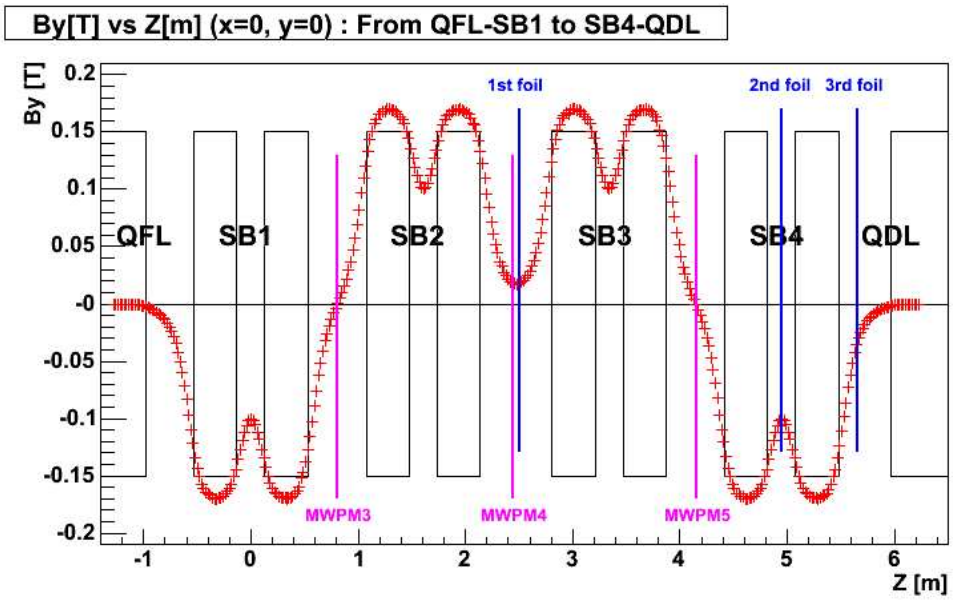

Figure 12: Distribution of magnetic field for shift-bump magnets. Red points show the measured magnetic field. Rectangles show the regions of magnets; lines, the locations of foils and MWPMs.

3 Beam commissioning based on virtual accelerator at the 3-GeV RCS

The VA presented here can simulate various kinds of measurements and it helps to construct the commissioning tools for the RA without using a real beam. In addition, the VA is capable of quickly identifying the faulty devices and optimization of ring optics and orbit with online when the beam behavior is different from expectations and simulations. The first beam-commissioning of the 3-GeV RCS started in September 2007. This section describes the result of the beam commissioning based on the VA at the 3-GeV RCS.

3.1 Beam control of injection line

We have constructed a commissioning tool for beam injection. The injection line is controlled by two ISEP magnets in the following. The detail overview of the injection line is described at Section 2.1.3. The main monitor is multi-wire profile monitor (MWPM). The injected-beam positions and widths for horizontal and vertical direction at the injection section are observed by the monitors. A response matrix A is obtained as $\Delta x_i = \sum A_{ij} \Delta\theta_j$, where Δx_i is the beam deviation at the i-th MWPM; $\Delta\theta_j$, the kick angle by the j-th ISEP; and

$$A = \begin{bmatrix} \partial x_3/\partial\theta_1 & \partial x_3/\partial\theta_2 \\ \partial x_4/\partial\theta_1 & \partial x_4/\partial\theta_2 \\ \partial x_5/\partial\theta_1 & \partial x_5/\partial\theta_2 \end{bmatrix}. \tag{3.1}$$

(3.2)

Further, the deviations at the MWPMs are related to beam position Δx_f and angle $\Delta x'_f$ at the 1st foil as

$$\begin{bmatrix} \Delta x_3 \\ \Delta x_4 \\ \Delta x_5 \end{bmatrix} = \begin{bmatrix} 1 & -L_3 \\ 1 & -L_4 \\ 1 & +L_5 \end{bmatrix} \begin{bmatrix} \Delta x_f \\ \Delta x'_f \end{bmatrix}, \tag{3.3}$$

where L_i is the length of the i-th MWPM from the first foil.
Using these equations and the position measurements at the MWPMs, the beam positions along the injection line should be adjusted to the design values, while the dump line DSEP settings are tuned by these equations using position measurements at the MWPMs located in the line.

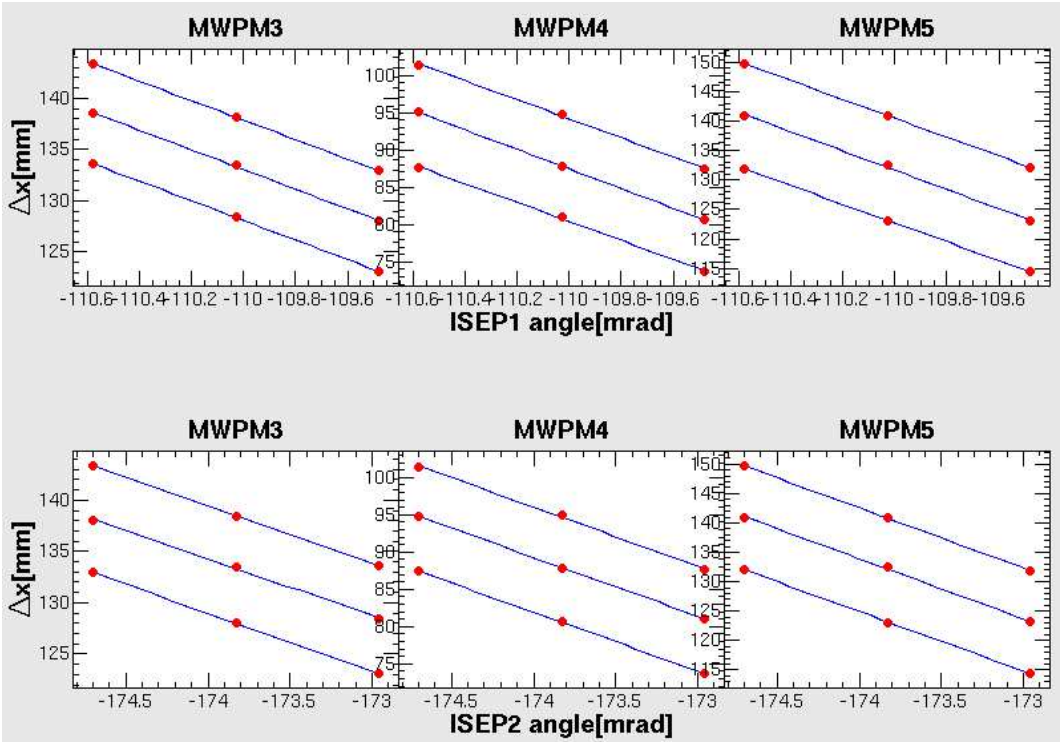

Figure 13: Beam Positions at MWMPs for kick angles of ISEPs in the RA

In the first commissioning, the injection beam line should make a match to the design orbit. In the case that the beam line has difference from the design orbit, the response matrix by the position measurements at the MWPMs for kick angle of ISEPs cannot be obtained from the view point of beam loss and aperture clearance. So, the response matrix is obtained by the same method on the VA and the beam positions to the designed ones at the MWPMs are controlled with a few iterations. The components of the matrix can be derived by the least square fitting of these data. The injection beam line needs to be optimized for the ring orbit instead of the designed beam line. After this procedure, the response matrix in the beam line was measured for the RA. The positions at MWPMs for ± 0.5 % of current kick angles were measured for the RA and the result is shown in Fig. 13. The OPI can select the response matrix by the VA or RA. The response matrix by the RA resulted in the precise control of the positions at MWPMs without the iteration. Since the VA has the same control procedure with the RA, the transition from the VA to the RA can only be performed by changing the selection of the record name and is very smooth. This function facilitates

the painting injection studies described in Section 4.

3.2 BPM polarity

In the RCS, 54 BPMs[20] are installed for the measurement of closed-orbit distortion (COD). The measured COD is corrected by 26 steering magnets. In the first commissioning, it is essential to check whether BPM's data are right or not. The displacements (Δx, Δy) of all BPMs were measured for kicks by some steering magnets in the RA and were compared with those in the VA. The sign of displacements was inconsistent for 18 BPMs, which implied the cable connections of these BPMs were reversed. Then, the polarities of these BPMs were corrected in the data processing stage hereafter. The beam-based alignment of the BPM will be performed in the future.

3.3 Measurement of betatron tune

A common method to measure the fractional part of betatron tune is to excite transverse beam motion and to detect the transverse beam position over a number of successive turns[19]. The betatron motion is excited by a single kick or white noise. If the beam has momentum spread and the ring has nonzero chromaticity, the betatron oscillations excited by a single kick will quickly fade away. Therefore, an exciter with band-limited white noise is installed in the RCS to excite coherent betatron motion and is then implemented in the VA. The exciter gives the beam a continuous kick by an electric field. The variable parameters of the exciter are the power and frequency range. For a frequency range of Δf_n, the expected value of coherent betatron amplitude is

$$x_{rms} \simeq \frac{\theta_{rms}\sqrt{\beta_x^e \beta_x^m}}{4} \frac{f_0}{\sqrt{\pi \Delta f_n \Delta f_b}} \tag{3.4}$$

where θ_{rms} is the rms kick-angle; β_x^e, the beta function at the exciter; β_x^m, the beta function at the monitor; f_0, the revolution frequency; and Δf_b, the rms value of the betatron tune spread. The kick angle is given by

$$\theta_{rms} \simeq \frac{eL}{pc}(1+\frac{1}{\beta})\frac{\sqrt{ZP}}{d} \tag{3.5}$$

where L is the electrode length; p, the momentum; e, the electron charge; β, the Lorenz factor; c, the speed of light; Z, the impedance of the deflector electrode; P, the output power of the exciter amplifier; and d, the distance between electrodes[21].

The BPM for tune measurement is installed in the nondispersive section of the ring and detects the transverse beam oscillation. The detected signal is analyzed by a discrete Fourier transform (DFT) package. The exciter parameters are adjusted so that the betatron tunes can be identified as the highest sideband peak of the revolution frequency.

The beam condition and the exciter's parameters for the tune measurement are examined by the VA. The chopped beam from the LINAC is captured in the RF bucket and the chopping factor is defined as the ratio of the chopped beam length to the RF bucket width and is equal to 0.56 in the normal condition. With the maximum output power of the exciter, 1 kW, we could not detect the tune peak of the beam in the normal chopping condition and without chromaticity corrections. We have found that the chopping factor should be less than 0.07 in order to clearly identify the tune peak. These consequences are taken into account in the tune measurements procedure

with the RA.

We constructed an OPI for the tune measurement. In the injection energy of 181 MeV at the RCS, the revolution frequency and sampling rate are 469 kHz and 6.4 MHz, respectively. The betatron-tune peaks are identified as the upper and lower sidebands of the revolution frequency peak. The OPI shown in Fig 14 has functions for identification of revolution-frequency peak and sideband peaks, calculation of betatron tune and the time fluctuation of the tune with a step of minimum 160 μsec from the beam injection to extraction. The fractional part of betatron tune can be calculated by

$$\nu = \frac{\mid f_{side} - f_{rev} \mid}{f_{rev}/h} \tag{3.6}$$

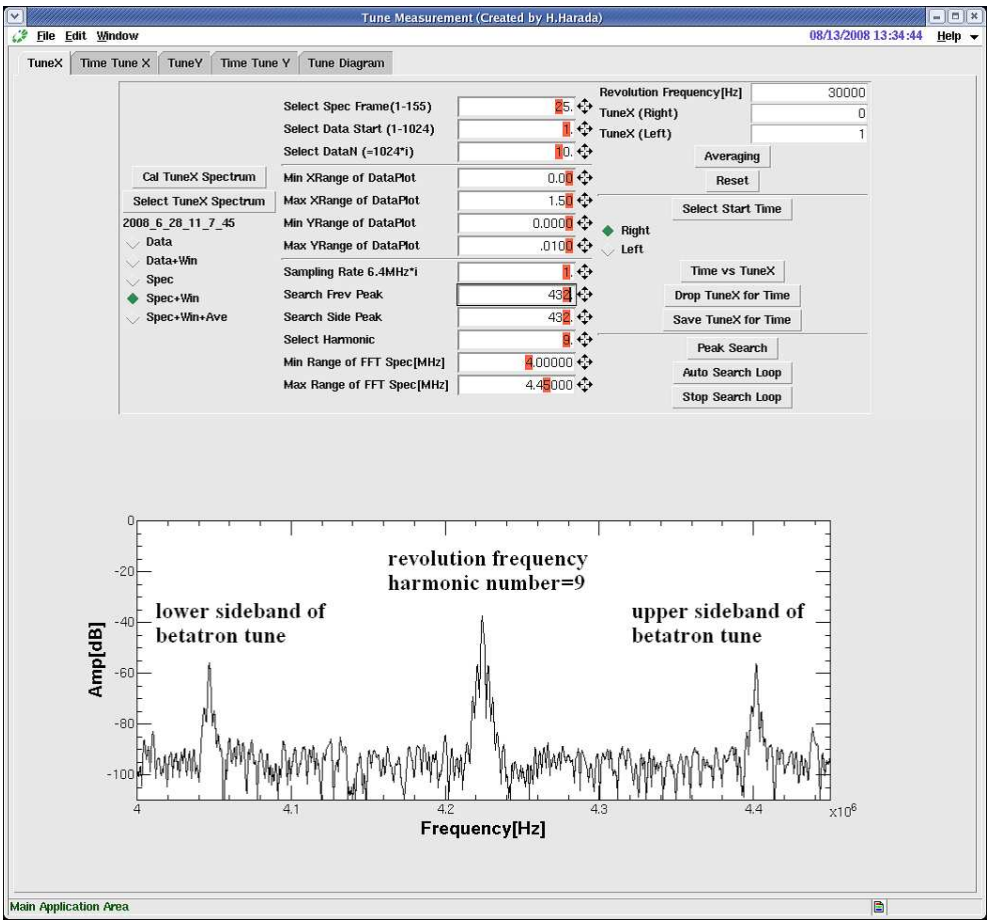

Figure 14: Operation Interface for measurement of betatron tunes

or

$$1 - \nu = \frac{\mid f_{side} - f_{rev} \mid}{f_{rev}/h} \tag{3.7}$$

where f_{side} is the frequency of the identified tune peaks; f_{rev}, the identified revolution frequency; and h, the harmonic number of the revolution-frequency peak. The plot in Fig 14 is the spectrum measured in the beam-storage mode (DC mode) of the RA where the chromaticity is corrected and the chopping factor is 0.11.

3.4 Measurement of chromaticity

The chromaticity ξ is defined by $\Delta\nu/(\Delta p/p)$, where $\Delta\nu$ is the betatron tune difference; Δp, the momentum difference; and p, the synchronous momentum.

The betatron tune is measured vs. beam momentum, where the momentum shift is created changing the RF frequency adiabatically. The chromaticity is then derived from the slope of the betatron tune with respect to its momentum[19]. A frequency shift Δf changes the beam momentum by an amount

$$\frac{\Delta f}{f} = \lambda \frac{\Delta p}{p}$$
$$\lambda = -(\alpha - \frac{1}{\gamma^2}) \tag{3.8}$$

where λ is the slippage factor; α, the momentum compaction factor; γ, the Lorenz factor; and f, the RF frequency for the synchronous particle.

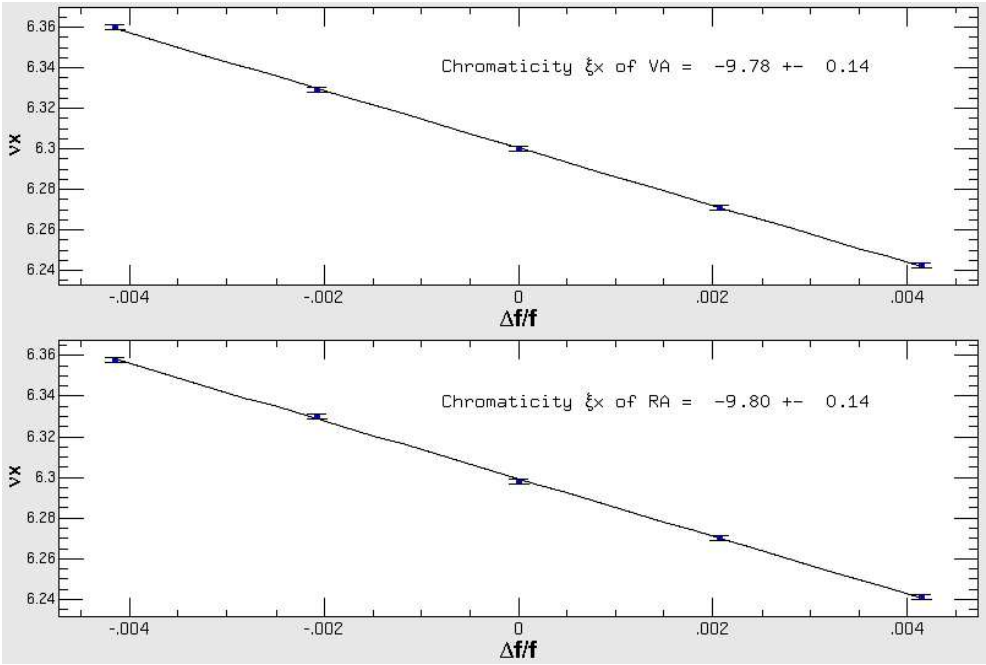

Figure 15: Frequency deviation $\Delta f/f$ versus fractional part of horizontal betatron tune ν_x in the VA (top) and RA (bottom)

We have virtually measured the betatron tune by changing $\Delta f/f$ from -0.00414 to 0.00414 in steps of 0.00207 in the beam storage mode. The RF frequency was changed adiabatically during the period from 2 to 10 msec after injection so that the particles do not dilute within the RF bucket, and a large portion of particles concentrates near the synchronous angle. Under these conditions, a betatron sideband peak can easily be obtained with the chopping factor of 0.07. The $\Delta f/f$ versus horizontal tune ν_x is shown in Fig.15. With the calculated slippage factor of -0.69, the horizontal and vertical chromaticities were -9.78 $\pm$ 0.14 and -6.89 $\pm$ 0.14, respectively. The error is due to the DFT resolution and the error of least square fitting. The results agree well with analytical calculations of ξ_x = -9.80 and ξ_y = -6.92. In the virtual measurements and analytical calculations, higher-order magnetic components were essential to produce such values, while the analytical chromaticities of only linear magnetic component are ξ_x = -8.35 and ξ_y = -8.39.

Based upon the good agreement, same procedure was applied to the measurements in the RA. After the optics corrections described in Section 3.7, the chromaticitiess were obtained to be -9.80 $\pm$ 0.14 and -7.03 $\pm$ 0.71 for the horizontal and vertical directions, respectively. The $\Delta f/f$ versus horizontal tune ν_x in the RA is also shown in Fig.15. The errors are estimated from the DFT resolution and the error of least-square fitting. The results agree well with them of analytical calculation and virtual measurement using the accelerator model with higher-order magnetic components.

3.5 Measurement of dispersion function

As one of optics parameters, the dispersion function η is defined by

$$\eta = \Delta z(s_i)/(\Delta p/p), \tag{3.9}$$

where s_i is the arc length of i-th BPM measured along the reference closed orbit; Δz, the closed orbit shift for either horizontal x or vertical y coordinate; Δp, the momentum difference; and p, the synchronous momentum.

We have virtually measured the COD at the 54 BPMs located around the ring by changing $\Delta f/f$ from -0.00414 to 0.00414 in steps of 0.00207 in the beam storage mode with calculated slippage factor of -0.69. The RF frequency was changed adiabatically the same procedure described in Section 3.4. The COD was measured after the frequency has been changed adiabatically, that is, 10 msec from the beam injection. From the results of virtual measurement, we understood that the COD for momentum shift has second-order term of $\Delta p/p$ in addition to the dispersion function of first-order term. Therefore, the dispersion function should be estimated from fitting function up to second-order term. Same procedure was applied to

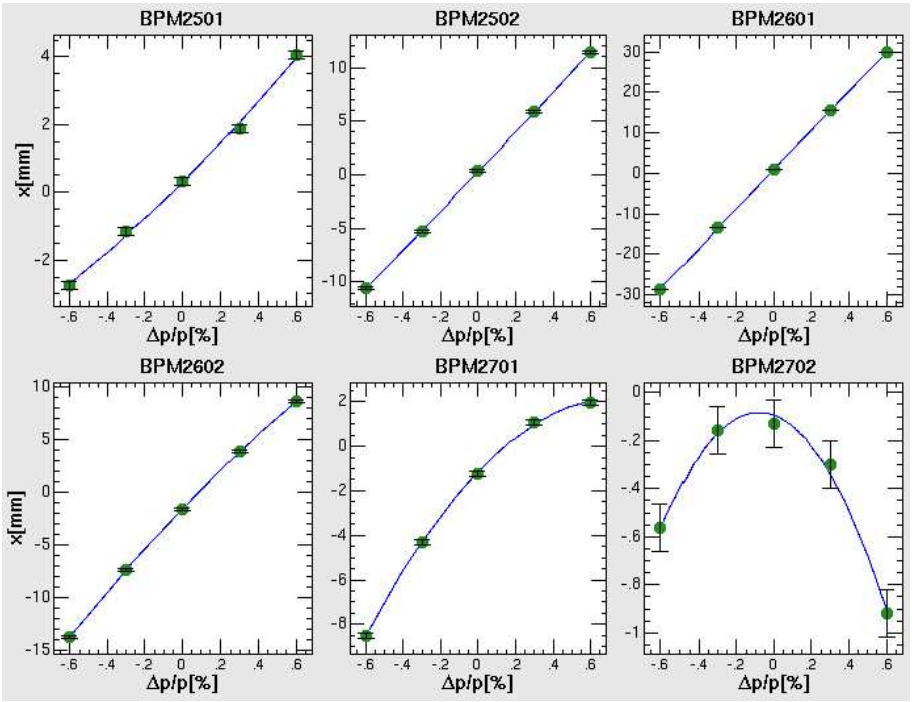

Figure 16: Momentum shift $\Delta p/p$ versus horizontal COD at six BPMs in the RA. Points and lines is the measured COD and the fitting result, respectively.

the measurements in the RA. The result for dispersive six BPMs located in the third arc section in case of operating tunes (6.30, 6.42) after optics correction described in Section 3.7 is shown in Fig 16. The COD is given the error bar of 0.1 mm as both BPM resolution and beam fluctuation pulse by pulse. The CODs for $\Delta p/p$ measured at 54 BPMs are fitted by fitting function up to second-order term and least-square method. The obtained dispersion functions and second-order terms in the ring are shown in Fig 17.

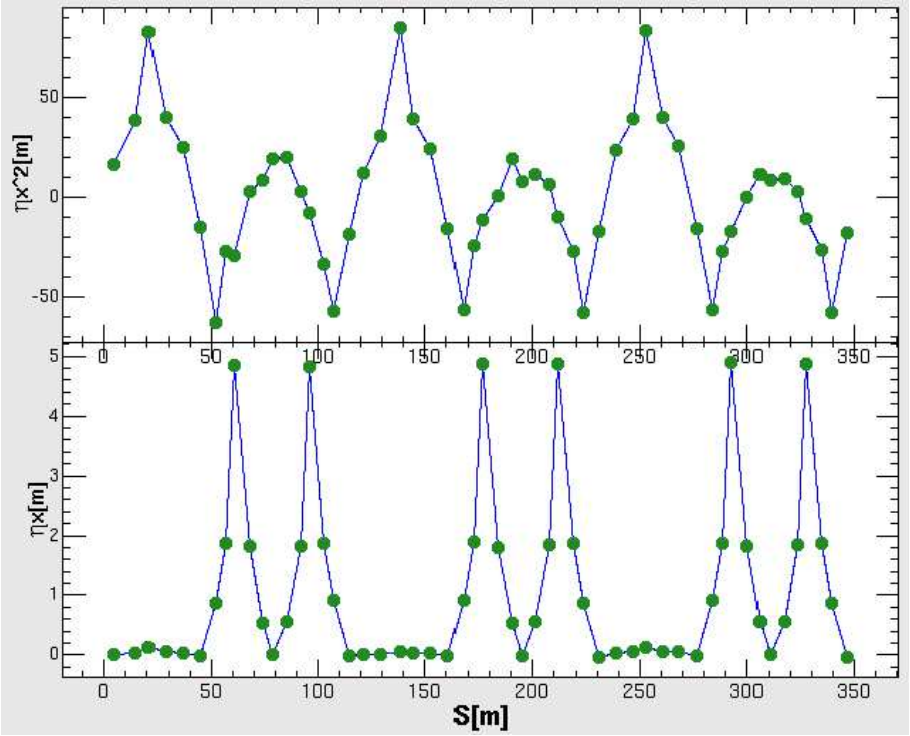

Figure 17: The obtained dispersion function(bottom) and second-order term(top) in the ring

3.6 Measurement of beta function

The beta function around the ring was estimated from the response of COD for a kick angle by the steering magnets. The closed-orbit shift on the i-th BPM by a kick angle of the j-th steering magnet is expressed as

$$\Delta z^j(s_i) = \frac{1}{2sin\pi\nu_z}\Delta\theta_z^j\sqrt{\beta_z(s_i)\beta_z(s_j)}cos(\pi\nu_z + \mid \psi_z(s_i) - \psi_z(s_j) \mid), \quad (3.10)$$

where s is the arc length measured along the reference closed orbit; Δz, the closed-orbit shift for either horizontal x or vertical y coordinate; ν, the betatron tune; β, the betatron function; $\Delta\theta$, the steering kick angle; and ψ, the betatron phase advance. In the RCS, most of BPMs are installed inside of the steering magnets and its betatron phase difference of each pair can be presumed to be negligible. Therefore, the betatron function $\beta_z(s_j)$ at each steering magnet in Eq. 3.10 is given as

$$\beta_z(s_j) = 2\frac{sin\pi\nu_z}{cos\pi\nu_z}(\frac{\Delta z^j(s_j)}{\Delta\theta_z^j}), \quad (3.11)$$

and the betatron function can be estimated from observable closed orbit response $\Delta z^j(s_j)/\Delta\theta_z^j$ and betatron tune ν_z. The closed orbit and betatron tune are directly measured with a sufficient accuracy. Our thin steering magnets with large gaps cause a large leakage field around their magnet edge. Therefore a part of the leakage field was absorbed by nearby components such as a quadrupole magnet. For this concern, several field measurements and simulations coupled with a quadrupole or steering magnet for several configurations were performed. As these results were in good agreement, we performed a series of field simulation for all the steering magnets and applied the simulated ones for the kick angle corrections. The simulated field reduction rates are 10-30% depending on their configurations.

3.7 Ring-optics control

Sixty quadrupole magnets are installed, consisting of 7 families. The set currents for the required focusing/defocusing strength are derived by the measured magnetic field. Further, some errors are unavoidable in the actual current setting and the field errors of quadrupole magnets cause the deviation of the optics parameters.

The betatron tune was directly measured by a method described in Section 3.3. The beta function was estimated from the response of COD for a kick by the steering magnets as described in Section 3.6. The dispersion function was estimated similarly for a momentum shift by the RF as described in Section 3.5. For these optics parameters independently measured, the differences between the designed and obtained parameters were clearly seen in Fig.18. Then, the VA calculated the strength of the quadrupole magnets to reproduce all of these measurements and betatron tune which was independently measured. The difference of the set and calculated values, which are called "fudge factor," are stored as a correction fcator in the VA. The fudge factors are several percent in the RCS. The optics parameters with corrected current setting agree very well with the measurements as shown in Fig.18 and parameters of quadrupole magnets for 1/3 ring are listed at Table 5. Presently, different fudge factors should be obtained when we largely move on to the different operation point. The VA gave the 3-GeV RCS the efficient and accurate control of the optics parameters, which are twiss parameters, dispersion functions and betatron tunes. Actually, the VA cut a time of this optics tuning from 3 days to 4 hours and the result leaded to examination of many ring-optics patterns during the limited beam-commissioning time.

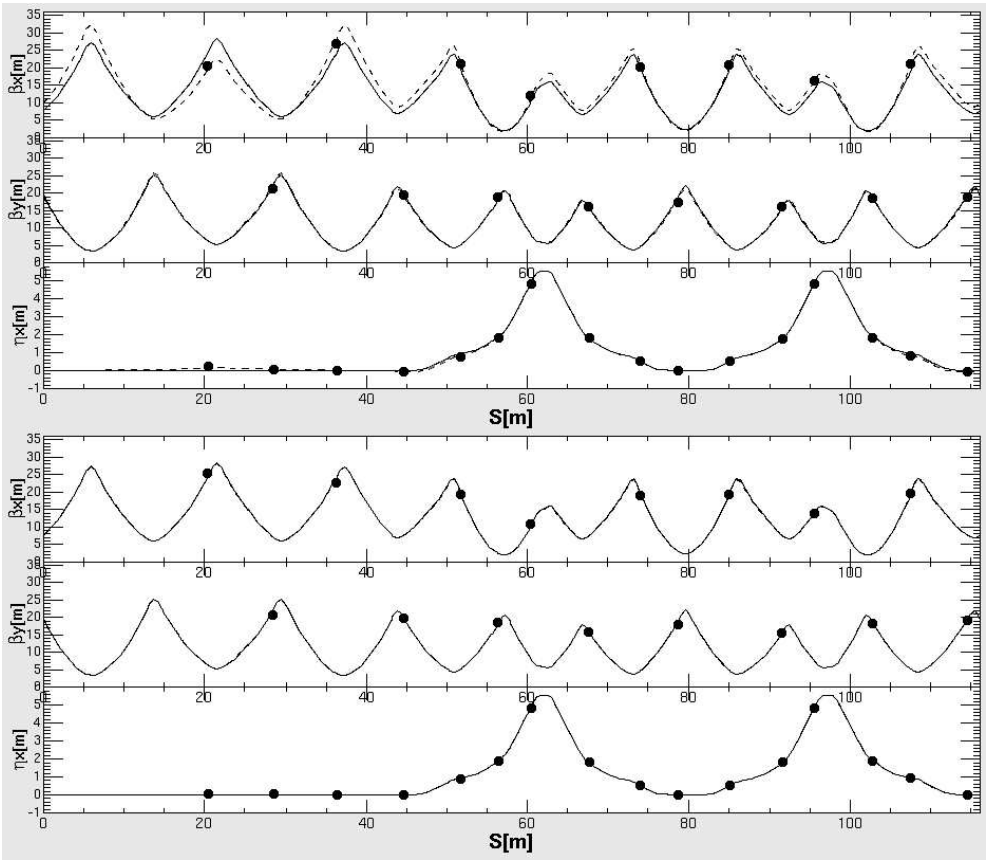

Figure 18: Optics parameters before (top) and after (bottom) corrections in one super period of the RCS. Beta function β_x for horizontal direction is plotted at the first trace; beta function β_y for vertical direction is plotted at the second trace; dispersion function η_x for horizontal direction, at the third trace. Solid lines are for design values; dots, for measured values at BPMs; and dashed line, for the VA calculations

Table 5: Parameters of quadrupole magnets for RCS 1/3 ring in case of (ν_x, ν_y)=(6.30, 6.42)

Name	K1$[m^{-1}]$	α_x	α_y	$\beta_x\,[m]$	$\beta_y\,[m]$	$\eta_x\,[m]$
QFL0101	0.17908	-2.42869	0.56004	26.06182	3.71497	-0.00138
QDL0101	-0.19799	0.67795	-2.60586	6.20874	23.91709	-0.00221
QFM0201	0.17305	-2.36717	0.57166	27.23331	5.54963	-0.00631
QDL0201	-0.19799	0.71771	-2.19799	6.24840	24.39019	-0.00255
QFL0301	0.17908	-2.27352	0.39513	26.24040	3.54935	-0.00162
QDX0301	-0.21390	0.95974	-2.52239	7.25770	20.82090	0.00062
QFN0401	0.23238	-1.96253	0.57225	23.47932	4.55333	0.79925
QDN0401	-0.23613	0.29989	-2.02847	1.97340	20.14412	2.06172
QFX0501	0.16040	-2.59333	1.35976	12.37362	6.84211	5.25514
QFX0502	0.16040	-0.71467	-0.01073	15.98709	5.69390	5.52093
QDN0501	-0.23613	0.91278	-2.22067	6.88310	16.90846	2.47128
QFN0601	0.23238	-2.15560	0.45513	23.22087	3.96579	0.78714
QDX0601	-0.21390	0.43738	-2.27793	2.42658	21.23513	-0.01669
QFN0701	0.23238	-3.15641	0.69114	22.33065	4.14875	0.63686
QDN0701	-0.23613	0.80881	-1.81582	6.80258	17.26900	1.97128
QFX0801	0.16040	-1.75318	1.11374	15.29555	6.38673	5.23410
QFX0802	0.16040	0.60893	-0.18582	14.50598	5.88983	5.53105
QDN0801	-0.23613	0.62322	-2.67366	2.22380	19.56955	2.54148
QFN0901	0.23238	-3.35887	0.66934	22.23729	4.62859	0.93600
QDX0901	-0.21390	0.67348	-1.99109	7.03465	21.29068	0.00098

4 Painting injection study for high-intensity operation

4.1 Identification of phase-space coordinates at injection point

Beam position and angle errors in transverse phase space at injection point produce betatron oscillation in the ring. In usual accelerator these errors are identified by various methods and are corrected to not have the oscillation. In the RCS, these errors need to be identified in order to discuss the painting injection process for the transverse direction with time varying in addition to correction of these errors. This section describes the identification method of the injection-beam displacement and angle for the ring orbit at injection point.

4.1.1 Phase-space coordinates at injection point by time-domain analysis

Beam motion in the ring can be detected by BPMs, which derive a beam position turn by turn or closed orbit distortion. If the position and angle turn by turn at BPM can be derived, the phase-space coordinates at injection point can be estimated by a transfer matrix from injection point to the BPM. The beam angle at BPM can be derived by selecting a BPM pair located at a drift space in the ring and the transfer matrix for optics in the ring can be calculated by the virtual accelerator. This method depends on the accuracy of the virtual accelerator in addition to that of BPM pair[22].

4.1.2 Phase-space coordinates at injection point by frequency-domain analysis

Injection-beam displacement and angle for the ring orbit at injection point cause the betatron oscillation in the ring. The oscillation can be detected as beam position at a BPM. In general, a given pair of conjugate phase-space coordinates at turn n is computed according to the matrix equation in the case that the beam motion is assumed to be linear,

$$\begin{bmatrix} \xi \\ \xi' \end{bmatrix}_n = \mathbf{M} \begin{bmatrix} \xi \\ \xi' \end{bmatrix}_{n-1}, \tag{4.1}$$

where ξ and ξ' is position and angle, respectively. The coordinates after n turns can be found by n successive applications of the matrix $\mathbf{M}$ to the initial coordinates. The resulting matrix after n turns can be parameterized according to

$$\mathbf{M}^n = \mathbf{I}\cos(n\omega_\xi T_0) + \mathbf{J}\sin(n\omega_\xi T_0), \tag{4.2}$$

$$\mathbf{I} = \begin{bmatrix} 1 & 0 \\ 0 & 1 \end{bmatrix}, \mathbf{J} = \begin{bmatrix} \alpha_\xi & \beta_\xi \\ -\gamma_\xi & -\alpha_\xi \end{bmatrix}, \tag{4.3}$$

where $\mathbf{I}$ is the identity matrix; $\mathbf{J}$, the matrix that contains the Twiss parameters; ω_ξ, the betatron tune; T_0, the ring revolution frequency. ξ denotes either the horizontal or vertical planes. The beam position $\xi(n, \omega_\xi)$ after n turns is

$$\xi(n, \omega_\xi) = \xi_0 \cos(n\omega_\xi T_0) + \{\alpha_\xi \xi_0 + \beta_\xi \xi_0'\} \sin(n\omega_\xi T_0), \tag{4.4}$$

where ξ_0 and ξ_0' are the initial coordinates. Eq. 4.4 indicates that the signature of the injection errors is cosinelike and sinelike oscillations in the time domain. In the frequency domain, the amplitude at the betatron oscillation frequency depends on the magnitude of the injection errors. Eq. 4.4 is transformed to the frequency domain using the discrete Fourier transform (DFT). The DFT of the sampled beam motion is given by

$$\Xi(\omega_m) = \sum_{n=0}^{N-1} \xi(n, \omega_\xi) e^{-jn\omega_m T_s}, \tag{4.5}$$

where the integer m is the frequency component; T_s, the sampling cycle, and $j = \sqrt{-1}$. The DFT component of the betatron oscillation is given by

$$\Xi(\omega_\xi) = \sum_{n=0}^{N-1} \xi(n, \omega_\xi) e^{-jn\omega_\xi T_s}. \tag{4.6}$$

DFT components of cosine-like and sine-like are

$$C(\omega_\xi) = \sum_{n=0}^{N-1} \cos(\omega_\xi T_0) e^{-jn\omega_\xi T_s}, S(\omega_\xi) = \sum_{n=0}^{N-1} \sin(\omega_\xi T_0) e^{-jn\omega_\xi T_s}. \tag{4.7}$$

The real and imaginary parts of Eq. 4.5 depend on these parts of the sine and cosine frequency-domain oscillation terms computed by Eq. 4.7. The real and imaginary parts therefore can be described by betatron response matrix $\mathbf{R}(\omega_\xi)$ and the initial coordinate as

$$\begin{bmatrix} Re[\Xi(\omega_\xi)] \\ Im[\Xi(\omega_\xi)] \end{bmatrix} = \mathbf{R}(\omega_\xi) \begin{bmatrix} \xi_0 \\ \xi_0' \end{bmatrix}, \tag{4.8}$$

where the response matrix is given by

$$\mathbf{R}(\omega_\xi) = \begin{bmatrix} Re[C(\omega_\xi)] + \alpha_\xi Re[S(\omega_\xi)] & \beta_\xi Re[S(\omega_\xi)] \\ Im[C(\omega_\xi)] + \alpha_\xi Im[S(\omega_\xi)] & \beta_\xi Im[S(\omega_\xi)] \end{bmatrix}, \tag{4.9}$$

and the symbols $C(\omega_\xi)$ and $S(\omega_\xi)$ are the complex cosinelike and sinelike oscillation in the frequency domain, and $Re[\ ]$ and $Im[\ ]$ denote taking the real and imaginary parts of a complex quantity.

The beam oscillation is detected by a BPM and the beam position ξ_i and angle ξ_i' at injection point are transformed to the initial coordinates by the transfer matrix $\mathbf{M}_{inj-bpm}$ from injection point to a BPM, and the transfer matrix is given by

$$\begin{bmatrix} \xi_0 \\ \xi_0' \end{bmatrix} = \mathbf{M}_{inj-bpm} \begin{bmatrix} \xi_i \\ \xi_i' \end{bmatrix}, \tag{4.10}$$

$$\mathbf{M}_{inj-bpm} = \begin{bmatrix} m_{11} & m_{12} \\ m_{21} & m_{22} \end{bmatrix}, \tag{4.11}$$

and the DFT components of the betatron oscillation for the phase-space coordinates at injection point is given by

$$\begin{bmatrix} Re[\Xi(\omega_\xi)] \\ Im[\Xi(\omega_\xi)] \end{bmatrix} = \mathbf{R}(\omega_\xi)\mathbf{M}_{inj-bpm} \begin{bmatrix} \xi_i \\ \xi_i' \end{bmatrix}, \tag{4.12}$$

and

$$\mathbf{M}_{res} = \mathbf{R}(\omega_\xi)\mathbf{M}_{inj-bpm}\,, \tag{4.13}$$

where $\mathbf{M}_{res}$ is the response matrix for the phase-space coordinates at injection point. The response matrix is uniquely fixed from optics in the ring. The phase-space coordinates at injection point can be derived from the DFT components and the inverse matrix of the response matrix for the betatron oscillation.

The components of response matrix can be obtained by measuring the responses of the DFT components for displacements of injection-beam position and angle changed independently. This method does not depend on a calculation of the beam simulator because the measured response matrix includes the information of Twiss parameters at a BPM and transfer matrix from injection point to a BPM. However, the independent control of beam position and angle at injection point with high accuracy is required.

4.2 Frequency spectrum of betatron oscillation

The beam oscillations are detected as the beam signal of four electrodes, which are defined as left, right, up and down for the beam direction, instead of the beam position turn-by-turn for horizontal and vertical direction. A BPM for betatron-tune measurements located at downstream of extraction section is used to detect the beam oscillations because only the BPM do not have a rotation for a beam direction and can independently detect the beam signal for horizontal or vertical direction.

We performed this measurement by the VA beforehand in order to know what parameters are important for this experiment with a good accuracy. From the result of the virtual measurement, the injection beam is requested the single intermediate pulse and peak current as high as possible for detection of betatron oscillations and enough beam signals in the ring. The injection-beam must always have the same timing for a trigger of data acquisition system and the same pulse-width because the phase-information of beam oscillation is different pulse-by-pulse. The effect of chromaticity must be as low as possible for keeping the initial amplitude of beta-oscillation by injection error. Therefore, the total voltage of RF cavities for a beam capture is as low as possible, and the momentum spread and synchrotron oscillation of captured beam have to be as low and slow as possible.

The conditions of the injection beam from LINAC on this experiment are listed in Table 6. The single pulse is chopped to time width with 0.56 μsec at LINAC and the time width corresponds to about half width of the RF bucket, which the harmonic number is 2. When the total voltage that the 4 RFs give to a beam is 68 kV, the time width corresponds to the momentum spread of about $\pm$ 0.8 % by synchrotron oscillation and the large spread causes the amplitude decay of betatron oscillation by the chromaticity. Therefore, we performed the decrease of effective voltage for a beam by the counter phasing between the RF cavities because a beam have the smaller momentum spread and later synchrotron oscillation. In case that each phase shift between cavities is 85 Degree and effective voltage is 4.7 kV, synchrotron-oscillation cycle is 200 turns and the momentum spread corresponds to $\pm$ 0.2 %.

The signals detected by electrodes of left and right is shown in Fig. 19. The

Table 6: Parameters of injection beam from LINAC

macro-pulse length [μsec]	2.13 (single pulse)
intermediate-pulse length [μsec]	0.56
peak current [mA]	25

betatron oscillation is clearly observed by the deference signal between the two electrodes. The deference signal detected in a time rage is calculated by DFT package and the obtained spectrum is shown in Fig. 19. The betatron-tune peak is identified as the sideband peak for the revolution frequency. The real and imaginary part of betatron oscillation component can be obtained.

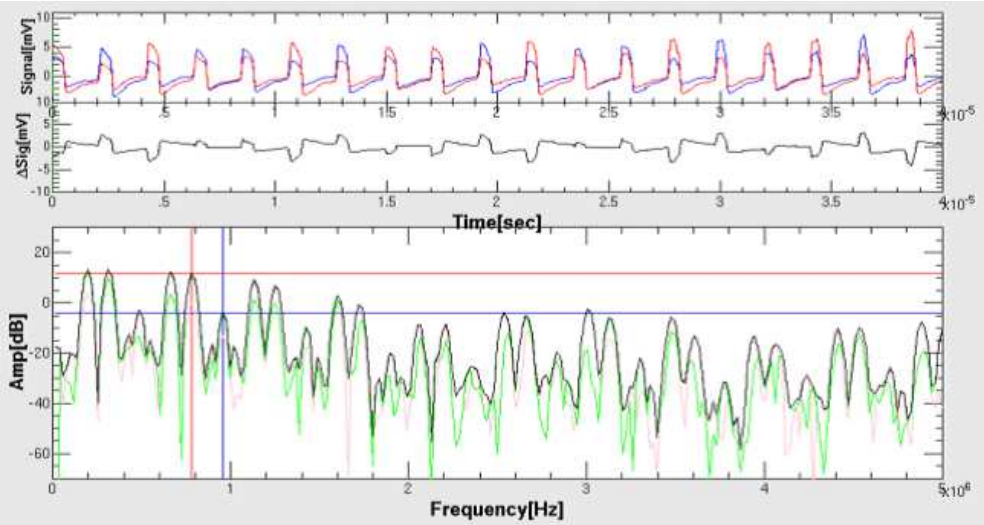

Figure 19: The top plot is the beam signal detected by left(blue) and right(red) electrode, the middle plot the deference signal between two electrodes, the bottom plot the frequency spectrum calculated by DFT package

4.3 Measurement of response matrix for frequency-domain analysis

The response matrix for the frequency domain described in section 4.1.2 were measured at the RCS. This section describes the detail method and the result of the matrix.

In the painting study, the operating point (ν_x,ν_y) of betatron tune is (6.38, 6.45). This point was searched by the tune survey and selected as a point of the low beam loss in high-current beam operation. During the response-matrix measurement and painting study, the beam optics does not change. So, the response matrix is constant.

The position and angle for horizontal direction at injection point are operated by the SB and ISEP magnet, respectively. The ISEP magnet can control the position only in short range from the aperture clearance. Therefore, the position was controlled by the bump-orbit height of the ring by SB magnet in order to cover the large range. The angle can be control by the ISEP magnet and the method is described in Section 3.1. The position and angle for vertical direction at injection point are operated by ISTMV magnet located in the injection line and the method is equal to case of ISEP magnet.

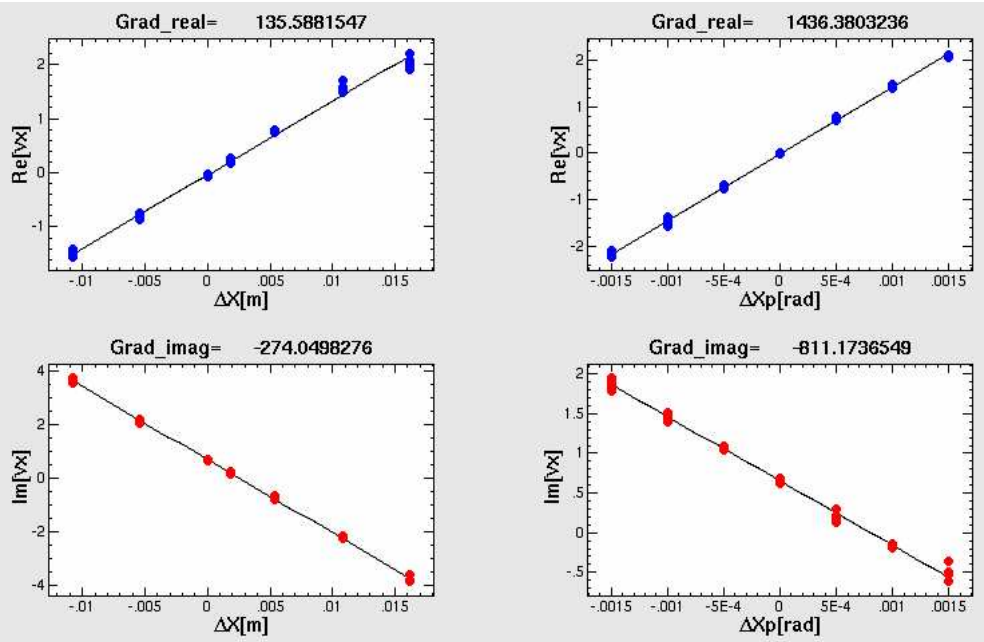

Figure 20: Real Re[ν_x](top) and imaginary Im[ν_x](bottom) parts of betatron oscillation for position Δx(left) and angle $\Delta x'$(right) at injection point

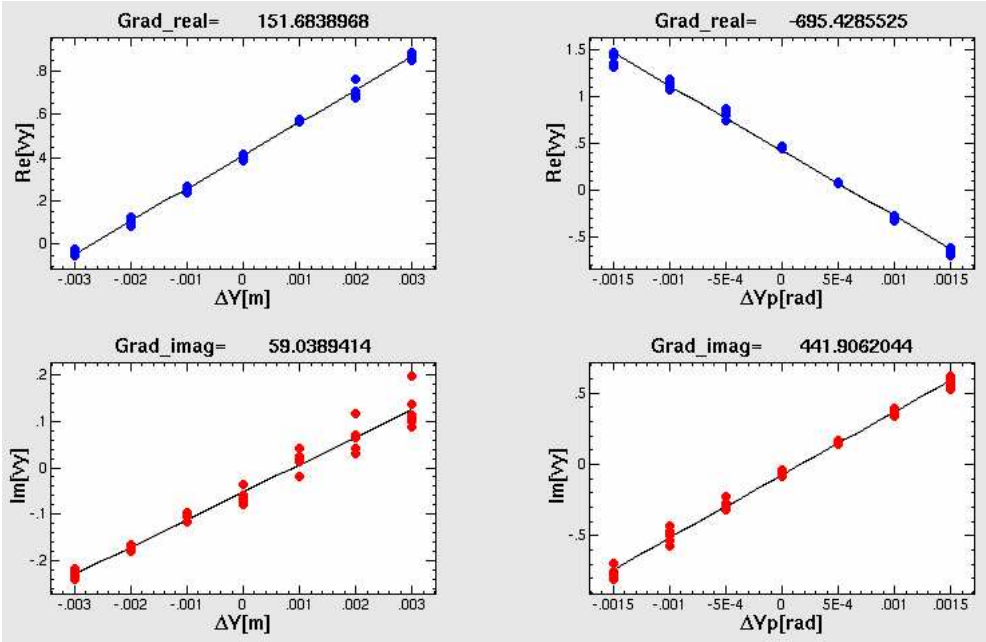

Figure 21: Real Re[ν_y](top) and imaginary Im[ν_y](bottom) parts of betatron oscillation for position Δy(left) and angle $\Delta y'$(right) at injection point

We got the real and imaginary part of betatron oscillation component with independently changing the position and angle, and the result for horizontal and vertical is shown in Fig. 20 and 21, respectively. The data of 5 points was gotten position by position, or angle by angle. The components of the matrix can be calculated these data by the least square fitting. As the result, the response matrix of betatron oscillation in the ring for horizontal and vertical direction are obtained.

4.4 Correction of injection errors using response matrix

The ring orbit has the COD so that the designed injection line has a mismatch for the orbit. This is called injection error. It needs to let the injection beam match to the bump orbit in the ring in order to perform the painting injection because the paint-bump orbit is built on the bump orbit created by the SB. Phase-space coordinates at injection point can be identified by the response matrix for a frequency domain. In this case, the identified values are position and angle for the ring orbit as injection error. In addition, the correction of injection error leads to check whether the response matrix can be used for painting-injection study.

We identified the position and angle for horizontal direction $(\Delta x, \Delta x')$ and vertical direction $(\Delta y, \Delta y')$ using the invariant matrix of the obtained response matrix. The injection error for horizontal and vertical direction was corrected by ISEP and ISTMV magnets, respectively. The mountain view of beam profile for horizontal and vertical direction detected by Ionization Profile Monitor (IPM)[23] before and after correction of injection error is

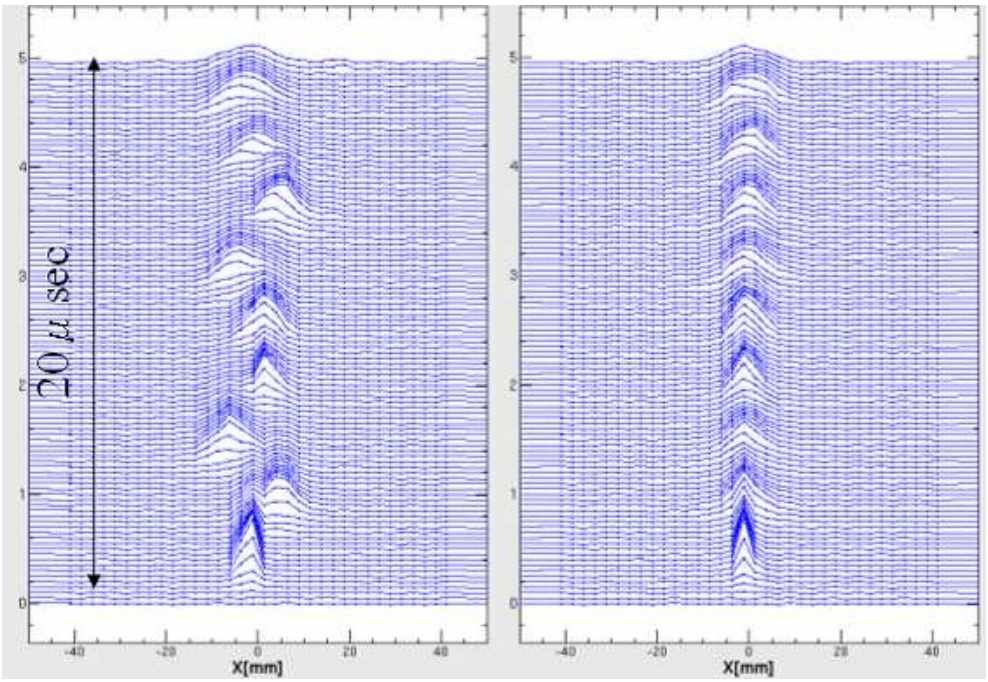

Figure 22: Mountain view for horizontal direction by IPM for 20μsec from beam injection before(left) and after(right) correction of injection error

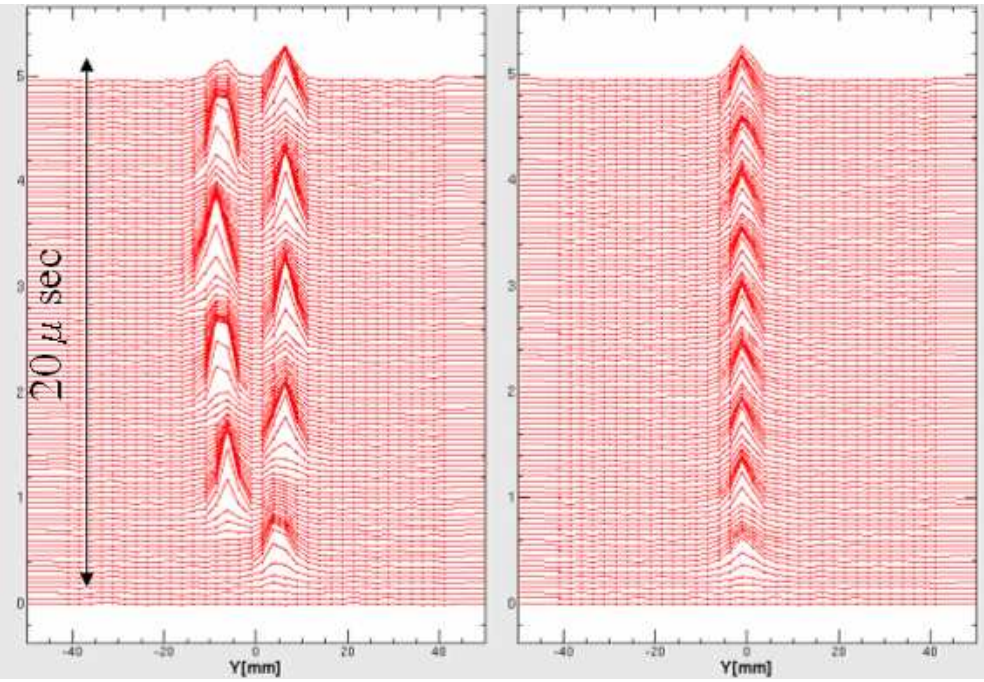

Figure 23: Mountain view for vertical direction by IPM for 20μsec from beam injection before(left) and after(right) correction of injection error

shown in Fig. 22 and 23, respectively. As shown in these figures, the beam turn by turn before the correction has a beta oscillation from the injection error. After just one correction, the beam didn't have the beta oscillation from the error. We got the response matrix for phase-space coordinate at injection point that it is possible to use for painting-injection study.

4.5 Definition of painting-injection area

The ring optics such as betatron tunes, twiss parameters and dispersion function, was controlled as described in Section 3.7. The ring optics of a real accelerator was reconstructed in the VA with accelerator model, and consequently the twiss parameters at injection point can be known from the VA. In a painting injection, the painting area is decided from the twiss parameters and required beam emittance in the ring, and the paint-bump orbit is decided from the painting area and the injection beam condition.

In the painting-injection study, the operating point (ν_x,ν_y) of betatron tune is (6.38, 6.45) and the twiss parameters of injection and circulating beam at injection point are listed in Table 7. The targeted painting-beam emittance of the ring is 100 $\pi mmmrad$. For horizontal direction, the paint-bump orbit (Δx, $\Delta x'$) for the shift-bump orbit is targeted to (31.1 mm, -4.4 mrad) at injection point. For vertical direction, the paint-bump orbit (Δy, $\Delta y'$) for the injection line is targeted to (0 mm, -1.9 mrad) at injection point.

Table 7: Twiss parameter of injection and circulating beam at injection point

Twiss parameter	injection beam	circulating beam
α_x	-0.33	1.71
$\beta_x[m]$	3.22	12.96
α_y	-0.23	-1.87
$\beta_y[m]$	4.81	12.37

Table 8: Parameters of quadrupole magnets for RCS 1/3 ring in case of (ν_x, ν_y)=(6.38, 6.45)

Name	K1$[m^{-1}]$	α_x	α_y	$\beta_x\,[m]$	$\beta_y\,[m]$	$\eta_x\,[m]$
QFL0101	0.19467	-2.74552	0.54240	27.86570	3.80237	0.00130
QDL0101	-0.19490	0.67682	-2.71709	4.84451	25.45425	-0.00511
QFM0201	0.19389	-2.26803	0.64585	23.29199	5.77272	-0.01983
QDL0201	-0.19490	0.47367	-2.31577	4.64160	25.91914	-0.00657
QFL0301	0.19467	-2.71956	0.48200	27.89577	3.74203	0.00049
QDX0301	-0.21718	1.04519	-2.43127	6.82919	20.30475	0.00490
QFN0401	0.21977	-1.74253	0.50597	20.49016	4.11910	0.81217
QDN0401	-0.23776	0.38028	-2.05244	2.76726	19.48017	2.12953
QFX0501	0.16096	-2.05751	1.30548	11.31592	6.90887	5.43561
QFX0502	0.16096	-0.32500	-0.06634	13.46600	5.96716	5.70793
QDN0501	-0.23776	0.72230	-2.39621	4.89171	18.19757	2.53686
QFN0601	0.21977	-2.15487	0.52225	20.00921	3.89275	0.73024
QDX0601	-0.21718	0.56657	-2.04711	4.35996	18.83168	-0.05588
QFN0701	0.21977	-2.24463	0.54614	19.92969	3.91133	0.57422
QDN0701	-0.23776	0.59278	-1.98343	4.79145	18.56537	2.01547
QFX0801	0.16096	-1.70392	1.22716	12.54766	6.76402	5.40908
QFX0802	0.16096	0.23313	-0.12202	12.84145	6.02946	5.72070
QDN0801	-0.23776	0.59816	-2.54061	2.93593	19.04520	2.62535
QFN0901	0.21977	-2.67115	0.60447	19.66750	4.19572	0.95316
QDX0901	-0.21718	0.51360	-2.02736	6.41536	20.66227	0.00590

4.6 Tuning of paint-bump magnets using the current pattern of flattop

We performed tuning of four horizontal paint-bump magnets (PB1-4) in the ring and two vertical paint-bump magnets (VPB1,2) in the injection line using the current pattern of flattop.

For horizontal direction, the tuning goal is to construct the closed paint-bump orbit with the target localized at injection area. The kick angle θ^i of the i-th PBs for the targeted bump orbit was calculated by the VA with parameters of the RA and the initial current I^i_{ini} was then derived from the result of magnetic-field measurement. If four horizontal paint bump magnets have the imbalance during the time they are on, the bump orbit is not closed and it causes the COD in the ring. The balance of horizontal paint-bump magnets was adjusted by the measured ring COD and the VA

Table 9: Current list of PBs. I_{ini} is PB's initial current; $\Delta I_{balance}$, PB's difference current for balance adjustment; I_{fix}, PB's final current set after all correction

Paint-bump magnets	I_{ini}	$\Delta I_{balance}$	I_{fix}
PB1	8.077 $[kA]$	-0.092 $[kA]$	8.871 $[kA]$
PB2	5.981 $[kA]$	0.112 $[kA]$	6.770 $[kA]$
PB3	1.993 $[kA]$	0.029 $[kA]$	2.247 $[kA]$
PB4	2.684 $[kA]$	-0.022 $[kA]$	2.958 $[kA]$

calculation. The result of balance adjustment as the ring COD is shown in Fig. 24. The paint-bump orbit at injection point was directly measured by the MWPMs after the injection beam matched to the bump orbit by the method described in Section 4.4. As the result, the paint-bump orbit (Δx, $\Delta x'$) for the shift-bump orbit is (28.12 mm, -3.96 mrad) for the target of (31.1 mm, -4.4 mrad) and the higher PBs's current by about 10 % was given by the VA calculation. The paint-bump orbit at injection point after the correction was directly measured by the MWPMs and it was (30.96 mm, -4.6 mrad) with good agreement. These parameters of PBs using for tuning are listed in Table. 9.

For vertical direction, the response of injection beam for the constant flat-top current of the VPBs obtained by the method such as one for the ISEPs described in Section 3.1. The currents of VPBs for the target (0 mm, -1.9 mrad) were derived from the response. The beam position in the injection line was directly measured by the MWPMs and consequently the bump orbit for vertical direction at injection point was (0.31 mm, -1.91 mrad) with good agreement.

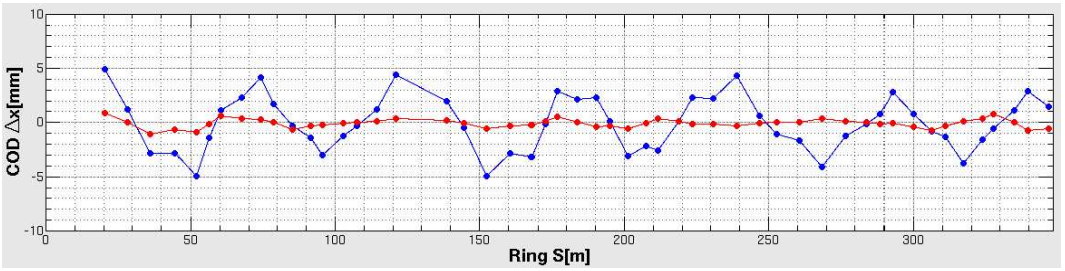

Figure 24: The measured ring COD before(blue) and after(red) balance adjustment of horizontal paint-bump magnets

4.7 Phase-space coordinates for current of paint-bump magnets

For a discussion of this painting-injection process, we identified the phase-space coordinates for current of paint-bump magnets with time varying. The current pattern of the magnets is changed within the beam-injection time of 500 μsec. The single intermediate pulse beams were injected by changing the injection timing for the shift- and paint-bump magnets with a step of 100 μsec and the phase-space coordinates for the timing at injection point were identified by the method discussed in Section 4.4. The result for horizontal and vertical direction is shown in Fig. 25. While the phase-space coordinates coincidentally measured at a BPM pair was transferred to the injection point with a transfer matrix obtained by the VA, the result for horizontal and vertical direction is shown in Fig. 26. On the phase-space coordinates at injection point, the beam seems to shift for a time on the long axis of an ellipse for horizontal direction and on the angle direction of an ellipse for vertical direction, and they are the expected bump orbit. These results independently obtained by the two methods would mean that the painting-injection process for transverse plane has been established.

We performed the multi-turn injection of 500 μsec with paint-bump magnets on and observed the beam profile by the Ionization Profile Monitor for horizontal (IPMH) and vertical (IPMV) direction. In order to discuss a beam profile from the effect of the painting injection, other sources to have an effect on a beam profile should be minimized as much as possible. The beam

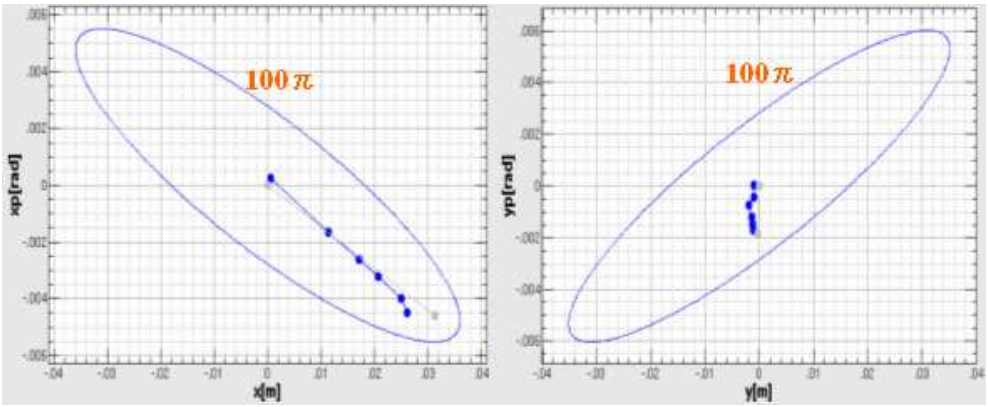

Figure 25: Horizontal(left) and vertical(right) phase-space coordinates for injection timing of 0, 100, 200, 300, 400 and 500 μsec by the frequency-domain method

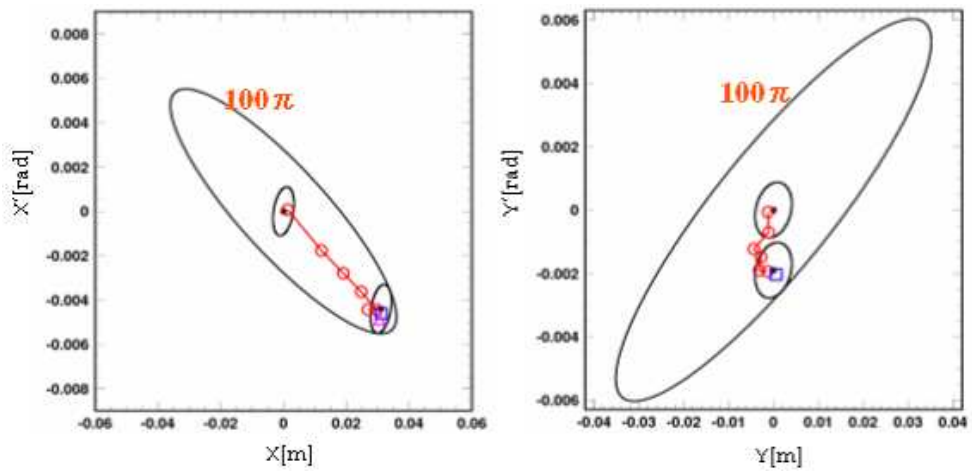

Figure 26: Horizontal(left) and vertical(right) phase-space coordinates for injection timing of 0, 100, 200, 300, 400 and 500 μsec by the time-domain method

current of 1 % for the rated current is requested for the same space-charge force on a center beam-injection. The IPMH is installed on the dispersive arc section and the momentum spread of a beam should be minimized as much as possible. Therefore, the chopped width of injection beam was changed to tithe of 560 nsec and this corresponds to the beam current of 1% for the rated current and the momentum spread of about ± 0.2 %. The mountain view of a beam profile for horizontal and vertical direction from 0 to 500 μsec observed by IPM is shown in Fig. 27. It means clearly that the beam profiles for horizontal and vertical direction were gradually increasing for the beam injection time.

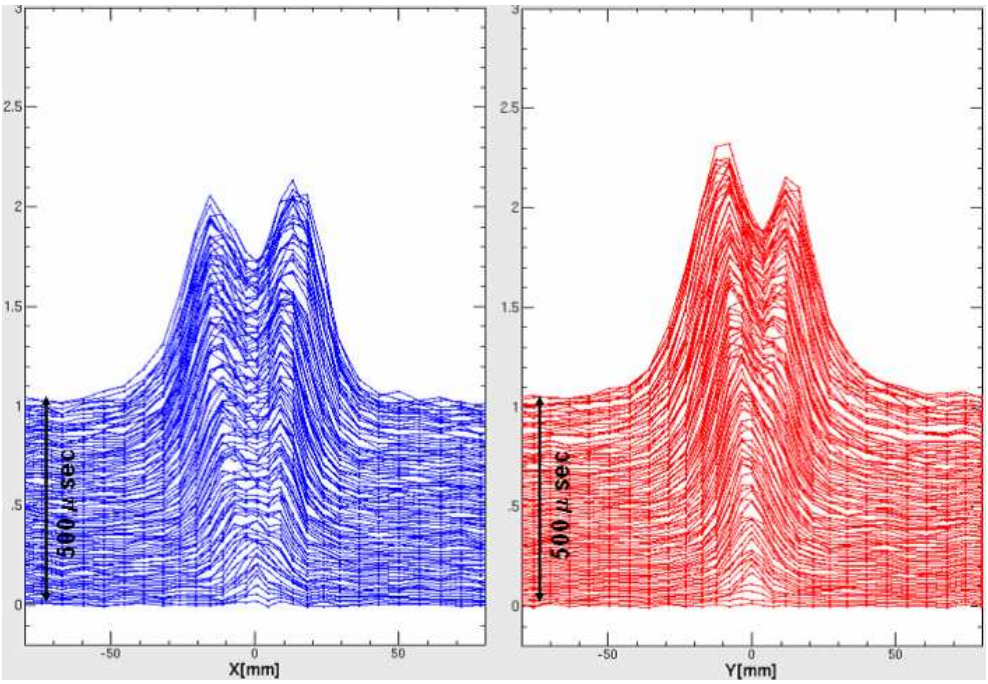

Figure 27: Horizontal(left) and vertical(right) beam-profile mountain-view for injection time of 500 μsec by IPM

5 Summary and conclusion

A new injection method has been originally developed and established during this doctoral research in Japan Particle Accelerator Research Complex (J-PARC) 3-GeV rapid-cycling synchrotron (RCS), whose the purpose is to provide a 1-MW proton beam. In such a high-intensity proton machine, it is essential to establish a method for stable operations while keeping the beam loss as low as possible. One of the challenging aspects for stable 1-MW provision is a large space-charge effect for density distribution of protons. The density control method in the transverse plane is principally focused in this doctoral research. The method which creates a uniform beam in the ring is called "painting injection". The painting injection performs the beam injection with sweeping the injection and the ring orbits, and fills the ring's elliptical phase-space at the beam-injection point from edge to center or from center to edge of the ring ellipse by the H^- injection beam whose emittance is small compared to the ring ellipse. The H^- beam is charge-exchanged at a carbon stripping foil and is injected to the ring. In painting-injection process, the foil is installed at the edge of ring ellipse in order to minimize the particle scattering of the circulating beam. The beam track control for horizontal and vertical phase-space coordinates is performed by eight horizontal paint-bump magnets installed in the ring and two vertical paint-bump magnets installed in the injection line. It is essential to accurately identify and control the ring parameters in order to precisely control the beam trajectories in the injection and the ring orbits, and to develop the method to identify these beam trajectories.

The virtual accelerator (VA) presented here is developed as an on-line accelerator model with beam diagnostic and is configured in the control system of the real accelerator for beam commissioning. The VA calculates the beam characteristics using real-accelerator parameters online. Commissioning tools based on the VA have been constructed for each commissioning stage. This control system with the VA enabled very efficient beam-commissioning activities such as decreasing debagging-time of these commissioning tools, examination of beam condition and scheme for variable parameter measurements, tuning/optimization of ring optics/orbit, and so on. The ring-optics for operating tune of (6.38, 6.45), which has been searched by a tune survey on low/high current operation, is controlled by the VA with a good accuracy. Consequently it defines the ring ellipse at the injection point and the beam trajectories of paint-bump orbits for the requested ring beam emittance of 100 π mm $mrad$ in the transverse plane.

We developed two schemes to derive the phase-space coordinates in order to identify the coordinates at the injection point in the painting-injection

processes. The betatron-oscillations due to the injection errors are analyzed in the time domain or the frequency domain in thesis scheme. The functionality of the schemes is verified by a matching between the injection and the ring orbits. The painting-injection process is tuned. If the four horizontal paint-bump magnets have imbalance during the painting injection, the bump orbit is not closed and a closed-orbit-distortion (COD) is generated in the ring. The balance of horizontal paint-bump magnets was adjusted by the measured ring COD and the VA calculation. The paint-bump orbit of (Δx, $\Delta x'$) is tuned to (30.96 mm, -4.6 mrad) for the target of (31.1 mm, -4.4 mrad) by the VA calculation. For the vertical direction, the response of injection beam for the constant current of the vertical paint-bump magnets (VPB) is obtained and the currents of VPBs are derived for the target (0 mm, -1.9 mrad). The obtained vertical coordinate at the injection point is (0.31 mm, -1.91 mrad), which agreed very well with the target value. During the painting-injection process, we identified the phase-space coordinates (paint-bump orbits) for current of paint-bump magnets, which agreed very well with the target trajectories. As the result, we have established the painting-injection method for the transverse plane.

In the RCS, the beam emittance and distribution can be controlled by this painting-injection scheme. Hence, this established painting-injection scheme will give an experimental approach for the study of the space-charge effect in rings such as benchmarks of simulation programs for multi-particle tracking with the space-charge force and studies of beam halos in high-intensity accelerators.

Acknowledgement

First I would like to express my great gratitude to my supervisor, Prof. K. Shigaki of Hiroshima University for his advice and full support during this thesis work. I am very honored to take a doctorate as his first student.

I would like to express my gratitude to Prof. T. Sugitate of Hiroshima University for his full support during this thesis work.

I am also deeply grateful to Prof. Y. Irie of High Energy Accelerator Research Organization (KEK) for his extensive advice, full support and detail discussion during this thesis work. His thoughtful, well-informed and educational suggestions lead all of this work to correct choices. His faithful and kind comments give me high motivation during this thesis work.

I would like to express my great gratitude to members of RCS beam-commissioning group, Dr. H. Hotchi, Dr. Y. Shoubuda and Dr. P.K. Saha of Japan Atomic Energy Agency (JAEA) for their educational advice, full support, detail discussion and tireless work during this thesis work and RCS beam commissioning. They give generously of their time to this thesis work any time day or night.

I would like to express my great gratitude to Mr. F. Noda of Hitachi Company for his advice and full support during this thesis work and RCS beam commissioning. His support leads to this work at J-PARC.

I would like to express my gratitude to Dr. S. Machida of Rutherford Appleton Laboratory, Prof. K. Furukawa of KEK, Dr. H. Sako of JAEA for extensive advice during development of virtual accelerator and work of refereed Journal paper.

I would like to express my gratitude to Prof. Y. Yamazaki of KEK, Dr. M. Kinsho and Dr. H. Suzuki of JAEA for full support during this thesis work at J-PARC.

I wish to appreciate Dr. T. Takayanaki, Mr. T. Ueno, Mr. K. Kanazawa and Mr. T. Togashi of JAEA for full support and detail discussion during work of the injection bump magnets and RCS beam commissioning.

I wish to appreciate Dr. M. Yoshimoto, Dr. J. Kamiya, Dr. M. Watanabe, Dr. Y. Watanabe and Dr. N. Tani of JAEA for support, advice and discussion about magnet operation during RCS beam commissioning.

I wish to appreciate Dr. N. Hayashi, Dr. K. Yamamoto, Mr. R. Saeki of JAEA and Dr. K. Satou of KEK for full support, detail discussion and kind advice about RCS beam monitor system during this thesis work and RCS beam commissioning.

I wish to express my thanks to Dr. F. Tamura, Dr. M. Yamamoto, Dr. M. Nomura of JAEA, Prof. M. Yoshii and Dr. C. Ohmori of KEK for full support, kind advice about RF system during this thesis work and RCS beam

commissioning.

I would like to express my gratitude to Prof. A. Ando, Prof. T. Koseki, Prof. N. Yamamoto, Dr. J. Takano, Prof. S. Igarashi and Prof. T. Toyama of KEK for kind support and detail discussion about beam commissioning during this thesis work and RCS beam commissioning.

I wish to appreciate Mr. H. Yoshikawa, Mr. H. Takahashi, Mr. M. Kawase, Dr. Y. Kato and Mr. Sakaki of JAEA for full support, detail discussion, kind advice about RCS control system and data acquisition during this thesis work and RCS beam commissioning.

I am grateful to Prof. K. Oide for his kind suggestions and comments during the course of this research.

I wish to appreciate Ms. Y. Nakano of JAEA and Ms. A. Haga of KEK for full support of working environment.

I would like to express my gratitude to Ms. M. Morinaga of Hiroshima University for full support of doctoral procedure.

I wish to appreciate Quark Laboratory crews for giving me happy life.

Finally, I express my greatest thanks to my parents for giving me a great deal of support, cheering me up at all times. I dedicate this thesis to my parents.

Figure 28: Commemorative photograph with J-PARC project staff when we have accomplished the beam acceleration up to the beam energy of 3-GeV at the 3-GeV RCS.

Appendix

A :Magnetic field expansion for deflecting magnet

The equations of motion are formed in the Cartesian coordinate system *(x, y, s)*, where x, y and s means a horizontal, vertical and beam-traveling direction, responsibility. We now assume symmetry in y only as the following.

$$\begin{aligned} B_y(y) &= B_y(-y) \\ B_x(y) &= -B_y(-y) \\ B_s(y) &= -B_s(-y). \end{aligned} \tag{A.1}$$

The field expansion is then given by

$$\begin{aligned} B_y &= \Sigma_{i,k=0}^{\infty} y^{2i} x^k a_{ik} \\ B_x &= z\Sigma_{i,k=0}^{\infty} y^{2i} x^k b_{ik} \\ B_s &= z\Sigma_{k,i=0}^{\infty} y^{2i} x^k d_{ik}. \end{aligned} \tag{A.2}$$

Maxwell's equations are

$$-\nabla \times \vec{B} = \{\frac{\partial B_x}{\partial s} - \frac{\partial B_s}{\partial x}, \frac{\partial B_s}{\partial y} - \frac{\partial B_y}{\partial s}, \frac{\partial B_y}{\partial x} - \frac{\partial B_x}{\partial y}\} = \{0,0,0\} \tag{A.3}$$

and

$$\nabla \cdot \vec{B} = \frac{\partial B_y}{\partial y} + \frac{\partial B_x}{\partial x} + \frac{\partial B_s}{\partial s} = 0. \tag{A.4}$$

From Maxwell's equations of Eqs. A.3 and A.4, the expansion coefficients are related by the following equations:

$$\frac{\partial B_x}{\partial s} - \frac{\partial B_s}{\partial x} = 0$$

$$\Sigma_{i,k=0}^{\infty} y^{2i+1} x^k b_{ik}\prime = \Sigma_{k,i=0}^{\infty} y^{2i+1} k x^{k-1} d_{ik}$$

$$b_{ik}\prime = (k+1) d_{i,k+1} \tag{A.5}$$

$$\frac{\partial B_s}{\partial y} - \frac{\partial B_y}{\partial s} = 0$$

$$\Sigma_{i,k=0}^{\infty}(2i+1)y^{2i}x^{k}d_{ik} = \Sigma_{k,i=0}^{\infty}y^{2i}x^{k}a_{ik}\prime$$

$$a_{ik}\prime = (2i+1)d_{ik} \tag{A.6}$$

$$\frac{\partial B_y}{\partial x} - \frac{\partial B_x}{\partial y} = 0$$

$$\Sigma_{i,k=0}^{\infty}y^{2i}kx^{k-1}a_{i,k+1} = \Sigma_{k,i=0}^{\infty}(2i+1)y^{2i}x^{k}b_{ik}$$

$$(k+1)a_{i,k+1} = (2i+1)b_{ik} \tag{A.7}$$

$$\frac{\partial B_y}{\partial y} + \frac{\partial B_x}{\partial x} + \frac{\partial B_s}{\partial s} = 0$$

$$\Sigma_{i,k=0}^{\infty}2iy^{2i-1}x^{k}a_{ik} + \Sigma_{k,i=0}^{\infty}ky^{2i+1}x^{k-1}b_{ik} + \Sigma_{k,i=0}^{\infty}y^{2i+1}x^{k}d_{ik}\prime = 0$$

$$2(i+1)a_{i+1,k} + (k+1)b_{i,k+1} + d_{ik}\prime = 0 \tag{A.8}$$

We need the field expansion of fourth-orders with y axial symmetry. B_y in Eq. A.2 is

$$\begin{aligned} B_y = {} & a_{00} + a_{01}x + a_{02}x^2 + a_{03}x^3 + a_{04}x^4 \\ & + a_{10}y^2 + a_{11}y^2x + a_{12}y^2x^2 + a_{20}y^4. \end{aligned} \tag{A.9}$$

When *i=0* and *k=0*, a_{10} in Eq. A.9 is exchange to the following by Eqs. A.5, A.6, A.7 and A.8.

$$a_{10} = -\frac{1}{2}(a_{00}\prime\prime + 2a_{02}) \tag{A.10}$$

When *i=0* and *k=1*, a_{11} in Eq. A.9 is exchange to the following by Eqs. A.5, A.6, A.7 and A.8.

$$a_{11} = -\frac{1}{2}(a_{01}\prime\prime + 6a_{03}) \tag{A.11}$$

When *i=0* and *k=2*, a_{12} in Eq. A.9 is exchange to the following by Eqs. A.5, A.6, A.7 and A.8.

$$a_{12} = -\frac{1}{2}(a_{02}\prime\prime + 12a_{04}) \tag{A.12}$$

When *i=1* and *k=0*, a_{20} in Eq. A.9 is exchange to the following by Eqs. A.5, A.6, A.7 and A.8.

$$a_{20} = \frac{1}{24}(a_{00}'''' + 4a_{02}'' + 24a_04) \tag{A.13}$$

In the result, we obtain the expansion B_y up to fourth-orders with y axial symmetry as the following.

$$\begin{aligned} B_y = a_{00} + a_{01}x + a_{02}x^2 + a_{03}x^3 + a_{04}x^4 - \frac{1}{2}(a_{00}'' + 2a_{02})y^2 \\ -\frac{1}{2}(a_{01}'' + 6a_{03})y^2x - \frac{1}{2}(a_{02}'' + 12a_{04})y^2x^2 \\ +\frac{1}{24}(a_{00}'''' + 4a_{02}'' + 24a_04)y^4. \end{aligned} \tag{A.14}$$

Using the same method, we obtain the expansion B_x and B_s up to fourth-orders with y axial symmetry as the following.

$$\begin{aligned} B_x = a_{01}y + 2a_{02}yx + 3a_{03}yx^2 + 4a_{04}yx^3 - \frac{1}{2}(a_{01}'' + 6a_{03})y^3 \\ -\frac{1}{2}(a_{02}'' + 12a_{04})y^3x \end{aligned} \tag{A.15}$$

$$\begin{aligned} B_s = a_{00}'y + a_{01}'yx + a_{02}'yx^2 + a_{03}'yx^3 - \frac{1}{6}(a_{00}''' + 2a_{02}')y^3 \\ -\frac{1}{2}(a_{01}''' + 6a_{03}')y^3x \end{aligned} \tag{A.16}$$

B :Transformation for Linear trajectory equations

The linear trajectory equations for deflecting magnet are

$$\begin{aligned} y'' + ky &= 0 \\ x'' - (k - \frac{1}{\rho^2})x &= -\frac{1}{\rho}\frac{\Delta p}{p_0} \end{aligned} \tag{B.1}$$

where ρ is the radius of curvature of the reference orbit; p_0, the momentum moving along the reference orbit; p, the particle momentum; and

$$k = \frac{e}{p_0}\frac{\partial B_y}{\partial x}\mid_{y=x=0} .$$

In a homogeneous deflecting field with $B_y = constant$, we have $k = 0$ and $1/\rho = constant$, and the linear trajectory equations B.1 are solved by

$$\begin{aligned} y(s) &= y_0 + y_0' s \\ x(s) &= x_0 cos\frac{s}{\rho} + x_0' sin\frac{s}{\rho} - \frac{\Delta p}{p_0}(1 - cos\frac{s}{\rho}). \end{aligned} \tag{B.2}$$

We assume the magnet has the entry and exit faces orthogonal to the reference orbit, an effective magnet length l along the reference orbit and an effective deflecting strength $1/\rho$ which is constant over this length. In this case, the magnet acts like a drift space of length l for the y component, while the transformation of the x component is given by

$$\begin{pmatrix} x \\ x' \end{pmatrix}_l = \begin{pmatrix} cos\varphi & \rho sin\varphi \\ -\frac{1}{\rho}sin\varphi & cos\varphi \end{pmatrix} \begin{pmatrix} x \\ x' \end{pmatrix}_0 + \frac{\Delta p}{p_0} \begin{pmatrix} -\rho(1 - cos\varphi) \\ -sin\varphi \end{pmatrix} \tag{B.3}$$

with $\varphi = \frac{l}{\rho}$.

We consider the fringe field at the magnet edge. For the x component, the transformation does not change. While the y component, the firing filed is slightly defocusing due to the deflection of the reference orbit in this region. With assuming the length of fringe field to $F1$ at entry and exit edges, the over-all transformation matrix of the magnet for the y direction is then given by

$$\begin{pmatrix} y \\ y' \end{pmatrix}_l = \begin{pmatrix} 1 & 0 \\ \frac{1}{6}\frac{F1}{\rho^2} & 1 \end{pmatrix} \begin{pmatrix} 1 & l \\ 0 & 1 \end{pmatrix} \begin{pmatrix} 1 & 0 \\ \frac{1}{6}\frac{F1}{\rho^2} & 1 \end{pmatrix} \begin{pmatrix} y \\ y' \end{pmatrix}_0 . \tag{B.4}$$

(B.5)

We consider the transformation of a homogeneous field magnet with arbitrary entry and exit angles ϵ_1 and ϵ_2, respectively. Such a magnet may be considered as a sector magnet with a "magnetic wedge," acting as a thin lens in each component, superimposed at each end. The x transformation has the form

$$\begin{pmatrix} x \\ x\prime \end{pmatrix}_l = \begin{pmatrix} 1 & 0 \\ -\frac{1}{\rho}tan\epsilon_2 & 1 \end{pmatrix} \begin{pmatrix} cos\varphi & \rho sin\varphi \\ -\frac{1}{\rho}sin\varphi & cos\varphi \end{pmatrix} \begin{pmatrix} 1 & 0 \\ -\frac{1}{\rho}tan\epsilon_1 & 1 \end{pmatrix} \begin{pmatrix} x \\ x\prime \end{pmatrix}_0 + \frac{\Delta p}{p_0} \begin{pmatrix} 1 & 0 \\ -\frac{1}{\rho}tan\epsilon_2 & 1 \end{pmatrix} \begin{pmatrix} -\rho(1-cos\varphi) \\ -sin\varphi \end{pmatrix}. \quad \text{(B.6)}$$

For the y component, we get

$$\begin{pmatrix} y \\ y\prime \end{pmatrix}_l = \begin{pmatrix} 1 & 0 \\ \frac{1}{\rho}\left(tan\epsilon_2 + \frac{1}{6}\frac{F1}{\rho cos\epsilon_2}\right) & 1 \end{pmatrix} \begin{pmatrix} 1 & l \\ 0 & 1 \end{pmatrix} \begin{pmatrix} 1 & 0 \\ \frac{1}{\rho}\left(tan\epsilon_1 + \frac{1}{6}\frac{F1}{\rho cos\epsilon_1}\right) & 1 \end{pmatrix} \begin{pmatrix} y \\ y\prime \end{pmatrix}_0. \quad \text{(B.7)}$$

References

[1] Y. Yamazaki ed., Accelerator Technical Design Report for High-Intensity Proton Accelerator Facility Project, JAERI-Tech 2003-044 and KEK Report 2002-13, 2003.

[2] L.J. Laslett, Proceedings of the 1963 Summer Study BNL 7534.

[3] EPICS home page, <http://www.aps.anl.gov/epics>.

[4] M. Ikegami, Transition from Commissioning to Operation in the J-PARC Linac, Proceedings of the High-intensity and High-brightness Beam Dynamics Work Shop (HB2008), Nashville, Tennessee, 2008.

[5] T. Koseki, Beam Commissioning of J-PARC MR, Proceedings of the High-intensity and High-brightness Beam Dynamics Work Shop (HB2008), Nashville, Tennessee, 2008.

[6] N. Tani *et al.*, Design of RCS Magnets for J-PARC 3-GeV Synchrotorn, IEEE Transactions on Applied Superconductivity, Vol.14, No.2, p.409 (2004).

[7] M. Yoshii *et al.*, Present Status of J-PARC Ring RF Systems, Proceedings of Particle Accelerator Conference (PAC2007), Albuquerque, New Mexico, 2007, p1511.

[8] M. Yoshimoto *et al.*, Present Status of Injection and Extraction System of 3 GeV RCS at J-PARC, Proceedings of European Particle Accelerator Conference, Edinburgh, UK, 2006, p.1765.

[9] K. Yamamoto *et al.*, Development of the Collimator System for the 3 GeV Rapid Cycling Synchrotron, Proceedings of Particle Accelerator Conference (PAC2005), Knoxville, Tennessee, 2005, p.1365.

[10] I. Sakai, S. Machida, F. Noda and Y, Irie *et al.*, H- Painting Injection System For The J-PARC 3-GeV High Intensity Proton Synchrotron, Proceedings of Particle Accelerator Conference (PAC2003), Portland, Oregon, 2003, p.1512.

[11] T. Takayanagi *et al.*, Measurement of the injection bump magnets at J-PARC 3GeV RCS, Proceedings of the 4th Accelerator Meeting in Japan, Wako, 2007.

[12] S. Hiroki *et al.*, Proceedings of Miti-Wire Profile Monitor for J-PARC 3-GeV RCS, Proceedings of European Particle Accelerator Conference (EPAC2008), Genoa, Italy, 2008, p.1753.

[13] SAD home page, <http://acc-physics.kek.jp/SAD/sad.html>.

[14] D. C. Carey and F. C. Iselin, A standard input language for particle beam and accelerator computer programs, Tech. Rep. CERN LEP-TH/84-10, European Lab. for Particle Physics, Geneva, Switzerland (June 1984), in Proc. Summer Study on Design and Utilization of the SSC, Snowmass, 1984, edited by R. Donaldson and J. G. Morfin, (Fermi National Accelerator Lab., Batavia, IL, 1985), p. 389.

[15] S. Wolfram, Mathmatica: A system for Doing Mathematics by Computer, Second Edition, Addison-Wesley Publishing Company, 1991.

[16] K. Ohmi, K. Hirata and K. Oide, From the beam-envelope matrix to synchrotron-radiation integrals, Phys.Rev.E49, 4474, 1994.

[17] Why Tcl?, <http://sunscript.sun.com/tcltext.html>.

[18] H. Hotchi, Private Communication.

[19] F. Zimmermann, Measurement and Correction of Accelerator Optics, in: SLAC-PUB-7844, Jun 1998, pp89.

[20] N. Hayashi *et al.*, The Status of the J-PARC RCS Beam Monitor System, Proceedings of the 5th Accelerator Meeting in Japan, Higashi-Hiroshima, 2008.

[21] T. Toyama, KEK-PS, Accelerator Study Note- 443, 2001, in Japanese.

[22] P.K. Saha *et al.*, to be published.

[23] K. Satou *et al.*, Beam Profile Monitor of the J-PARC 3GeV Rapid Cychling Synchrotron, Proceeding of European Particle Accelerator Conference (EPAC2008), Genoa, Italy, 2008, p.1275.